Nuclear Engineering and Technology 57 (2025) 103604

Contents lists available at ScienceDirect

Nuclear Engineering and Technology

journal homepage: www.elsevier.com/locate/net

Original Article

Electric double layer and thermal radiation effects on micropolar blood particles conveying Cu-MoS_2 -CuO nanoparticles in squeezed arterial channel

A.M. Obalalu [a], Umair Khan [b,c,*], Mehboob Ul Hassan [d], Muhammad Waqas [e], A.D. Adeshola [a], Latif Ahmad [f]

[a] Department of Mathematics and Statistics, Kwara State University, Malete, Nigeria
[b] Department of Mathematics, Saveetha School of Engineering, Saveetha Institute of Medical and Technical Sciences, Saveetha University, Chennai, 602105, Tamil Nadu, India
[c] Department of Mathematics, Faculty of Science, Sakarya University, Serdivan, Sakarya, 54050, Turkey
[d] Department of Economics, College of Business Administration, King Saud University, Riyadh, Saudi Arabia
[e] Department of Mathematics, City University of Science and Information Technology, Peshawar, Pakistan
[f] Department of Mathematics, Shaheed Benazir Bhutto University, Sheringal Upper Dir, 18000, Pakistan

ARTICLE INFO

Keywords:
Squeezed arterial channel
Ternary nanofluid
Rotational motion
Electric-double layer
Poisson-Boltzmann equation

ABSTRACT

The rotational motion of the blood particles in the squeezed arterial channel is important for advancing biomedical applications such as targeted drug delivery and diagnostic devices. In the present framework, we study the rotational motion of the blood particles and electric double layer (EDL) flow containing molybdenum disulfide (MoS_2), copper oxide (CuO), copper (Cu) ternary nanofluid in an arterial squeezed channel. To enhance the model's novelty, the Poisson-Boltzmann equation is utilized with the Debye-Hückel approximation to estimate the electric potential accurately. Also, we explore the impact of thermal radiation mechanisms along with thermal slip and heat sources to better understand heat transfer phenomena. The arising differential system composed of momentum, and temperature equations is treated through a numerical approach called the finite element method. Results demonstrate that an increase in the Hartmann number leads to a reduction in velocity profiles by up to 30 %, while a higher zeta potential parameter enhances flow velocity by 15 %. Additionally, microrotation of blood particles increases by 20 % with elevated vortex viscosity. Thermal radiation significantly improves heat transfer rates, as evidenced by an 18 % rise in the Nusselt number under intensified thermal slip conditions. These findings present critical insights for optimizing biomedical flows and heat transfer mechanisms in engineering applications.

1. Introduction

Research on micropolar blood flow has attracted significant interest due to its numerous industrial applications and important effects on several technical processes. These applications cover various fields, including biomedical engineering, nanotechnology, and microplasma devices. The research of blood dynamics via micropolar liquid theory, recognized as micropolar blood flow, offers a nuanced understanding that extends beyond the classical Newtonian approach. This approach takes into account the rotational motion of fluid elements, incorporating microstructural characteristics that distinguish it from traditional Newtonian fluids. Micropolar fluid models are characterized by additional material properties related to micro-rotation, providing a more comprehensive description of fluid behavior, especially in the presence of small-scale rotational phenomena [1]. Cheng et al. [2] studied the use of a polarized micropolar nanofluid to create a 2D time-dependent radiative flow of blood using titanium dioxide particles across an extended, curved plate. It is observed that whereas the velocity profile displays a reverse pattern, the micro-rotation and temperature field demonstrate a falling trend with higher substantial parameters. Ferdows

* Corresponding author. Department of Mathematics, Saveetha School of Engineering, Saveetha Institute of Medical and Technical Sciences, Saveetha University, Chennai, 602105, Tamil Nadu, India.
E-mail addresses: adebowale.obalalu17@gmail.com (A.M. Obalalu), umairkhan@sakarya.edu.tr (U. Khan), mehassan@ksu.edu.sa (M.U. Hassan), waqasmathematics@gmail.com (M. Waqas), adeshola.dauda@kwasu.edu.ng (A.D. Adeshola), latifahmad@sbbu.edu.pk (L. Ahmad).

https://doi.org/10.1016/j.net.2025.103604
Received 4 December 2024; Received in revised form 30 January 2025; Accepted 22 March 2025
Available online 3 April 2025
1738-5733/© 2025 Korean Nuclear Society, Published by Elsevier Korea LLC. All rights are reserved, including those for text and data mining, AI training, and similar technologies. This is an open access article under the CC BY-NC-ND license (http://creativecommons.org/licenses/by-nc-nd/4.0/).

and Liu [3] introduced a computational analysis of spontaneous convective motion involving an electrically conductive, viscous, micropolar fluid passing adjacent to a vertical surface. Kumar Yadav et al. [4] examined the movement of a micropolar/Eringen fluid confined between two layers of Newtonian fluid within a porous horizontal conduit. Kumar et al. [5] showcased fluid flow and heat transfer characteristics in the hydromagnetic micropolar fluid caused by elongating a surface with a second-order velocity slip. The expected effects of nonlinear radiation were considered. Solutions are concurrently provided for both first and second-order velocity slip conditions. Khader and Sharma [6] investigated the influence of an irregular heat source/sink and thermal radiation on the transient magnetohydrodynamic (MHD) micropolar fluid motion on a stretching/shrinking sheet. Recent and innovative contributions to the understanding of micropolar fluid can be seen in Refs. [7–10].

Thermal radiation has become increasingly significant in the fields of medicine and industrial processes due to its distinct characteristics and potential applications. Also, thermal radiation is of significant importance as heat is exchanged through a combination of conduction and convection within the fluid. Salawu et al. [11] considered various factors such as the non-uniform solar radiation of aircraft wings and the combination of copper and cobalt ferrite nanoparticles in a base fluid consisting of glycol. The mobility of hybrid CNTs around a rotating sphere when there is heat radiation and thermophoretic particle deposition at the stagnation point was assessed by Ramesh et al. [12]. Nanotechnologies with efficient heat-generating or absorbing capabilities have been found by Wang et al. [13] and have a variety of uses in mechanical design. Dolui et al. [14] scrutinized the theoretical impact of ternary hybrid nanoparticles (Cu-Ag-Au) on blood flow in two dimensions with a slanted catheterized artery with multiple stenosis and wall slides. Innovative results were obtained when nonlinear thermal radiation and an induced magnetic field from the outside were coupled. The outcomes of a mathematical model for time-dependent MHD boundary layer flow with the influence of a heat source across a porous stretched surface were computationally analyzed by Mukhtar et al. [15]. The study of thermal radiation in fluid dynamics is essential for a comprehensive understanding of heat transfer phenomena, especially in situations involving high temperatures, combustion, or special fluid characteristics. It often requires a combination of fluid dynamics and heat transfer analysis, including radiative heat transfer models, to accurately describe and predict the behavior of the system under consideration [16,17].

The magnetic effect is referred to as magnetohydrodynamics (MHD) or hydro-magnetics phenomenon that explores the interplay between magnetic fields and fluid behavior. This phenomenon seeks to comprehend the impact of magnetization which can alter the motion and behavior of fluids. This field of study is utilized in a diverse array of scientific fields spanning from engineering to astronomical research. MHD is also used in power-generating systems, in which a conductive fluid combines with a magnetic field to generate energy. MHD concepts are also applied in electromagnetic launchers such as rail guns to accelerate projectiles without the need for chemical propellants [18]. The influence of varying viscous flow within a compressing channel was studied by Chu et al. [19]. They mixed silver and gold hybrid nanofluid particles of varied forms into engine oil's base fluid. The research looked at the flow and heat transmission processes in the MHD regime between two parallel infinite plates. The goal of Mandal et al. [20] was to quantitatively investigate the effect of numerous geometric factors on a unique W-shaped porous cavity subjected to hybrid nanofluid-based MHD mixed convection. The W-shaped cavity is differentiated from the traditional trapezoid cavity in that it has a triangular form at its bottom. At a curve-extending surface, the MHD extended flow of second-grade viscoelastic nanofluid was explored in two dimensions. Joule heating and curvature parameters were previously used to examine heat transfer and velocity of mass transfer were study by Ref. [21]. Bhatti et al. [22] delved into the unsteady flow restricted by rotating circular plates with opposing motion in a permeable medium comprised of Williamson nanofluid. The range of mechanical mechanisms included by circular plates contributed to their relevance. These flow patterns were systematically significant in preventing friction, rotating equipment, the development of crystal techniques, and viscometry. The Williamson fluid model contained nanoparticles and motile gyrotactic microbes. It is expected that increasing the capacity of the elements utilized for total thermal energy preservation will increase their efficiency. Arshad et al. [23] evaluated the heat conduction phenomena of hybrid phases along with biphasic spinning nanofluid flow in a 3D domain through a stretchable surface with the impact of a magnetic field. Gasmi et al. [24a,b] assessed the influence of chemical diversity on the velocity of biphasic motion and incompressible liquids flowing between parallel spinning plates with the sheets thermally uniform and electrically insulated. The impact of the magnetic field on combined convection heat exchange with Casson fluid flow through a porous surface in the framework of thermal diffusion processes involving carbon nanotubes (CNTs) was scrutinized by Al-Turef et al. [25]. Dawar et al. [26] investigated hybrid nanofluid (magnetized/non-magnetized) flow in the presence of gyrotactic microbes across a layered stretched sheet. Kumar et al. [27] researched the consequences of chemically reactive components and heat generation on MHD blood circulation in porous bifurcated arteries, taking into account a tilted magnetic field. Electrically conducting materials experience the Hall effect when a magnetic field is exerted orthogonal to the current propagation. The flowing charged ions deflect to the opposite end of the conductor when electric current flows through the material under the exerted magnetic field. Consequently, a voltage difference identified as the Hall current emerges along the conductor's width that is orthogonal to the alternating current and the magnetic field. MHD is important for comprehension of the Earth's magnetic field, geophysical storms, associations with solar radiation, and researching celestial magnetic fields and space weather phenomena. MHD is also used in power-generating systems, in which a conductive fluid combines with a magnetic field to generate energy. It is being identified to use salt water for space propulsion and electrical power generation. MHD concepts are also used in electromagnetic launchers such as rail guns to accelerate projectiles without the need for chemical catalysts. A finite element analysis of laminar unsteady flow of viscoelastic fluids through channels with non-uniform cross-sections were study by Ref. [28]. Computational model on pulsatile flow of blood through a tapered arterial stenosis with radially variable viscosity and magnetic field were study by Ref. [29]. Analysis of pulsatile blood flow through stenosed arteries and its applications to cardiovascular diseases were study by Ref. [30]. Thermal performance and MHD peristaltic flow of hybrid nanofluid (Au-Ta/Blood) in an asymmetric conduit with electro-osmosis and shape factor effects were study by Ref. [31]. Electro-Osmotic Mechanism of Ellis fluid with joule heating, viscous dissipation, and magnetic field effects in a pumping microtube were study by Ref. [32]. Sensitivity analysis on electro-osmotic flow of EMHD tangent hyperbolic nanofluid through porous rotating disk with variable thermal conductivity, Stefan blowing and thermal radiation were study by Ref. [33].

The popularity of hybrid nanofluids (HNFs) has experienced a significant surge over the past few years. Hybrid nanofluid refers to a novel class of advanced fluids assembled by infusing nanoparticles of various kinds into a base fluid. The resulting mixture exhibits remarkable properties and synergistic effects due to the combination of unique features from each constituent [32]. Huminic [33] provided an overview of findings on entropy generation, specifically HNFs in numerous kinds of heat sources with varying physical configurations and boundary conditions. They reported that if 0.1 % (Graphene nano-platelets) was mixed in at 60 °C, the greatest heat transfer rate of the base fluid was 23.74 %. At all concentrations and temperatures ranging from 30 to 50 °C, HNFs maintained greater thermal conductivity compared to mono nanofluid. Waini et al. [34] modified the heat transfer in a steady flow of HNFs over a porous shrinking/stretching wedge by reviewing the special impact of thermal radiation. As a result, their research

demonstrated that the hybrid nanofluid surpasses the ordinary nanofluid in terms of increasing heat transfer rate. According to Khan et al. [35], empirical models concerning energy consumption have been established to illustrate the system limits under various cooling circumstances. The functionality of mono and hybrid nanofluids was tested by accessing the viscosity and coefficient of friction. Furthermore, the analyzed outcomes have been subjected to comprehensive long-term viability. Abbas et al. [36] employed the Yamada-Ota model and the Xue model for HNFs to explore the flow at the stagnation point with an inclined orientation applied magnetic field across an oscillating sheet. Madhukesh et al. [37] employed a non-Fourier heat flux model to examine the flow of HNFs across an irregularly stretched surface. Their findings compared the implications of Newtonian heating on a hybrid nanofluidic channel. As a result, to overcome that gap, they also concentrated on the consequence of significant parameters over the fluid properties of nanofluid-based hybrids inside the boundary layer. Sadeghi et al. [38] presented the antimicrobial characteristic of a hybrid nanofluid for removing germs while also utilizing its magnetic potential to increase the heat transmission rate. Mourad et al. [39] conducted a computational analysis of heat transmission and steady MHD natural convection in a cooler and permeable container with curved walls and an elliptical interior tube that contained a hybrid Fe3O4-MWCNT/water nanofluid. The changing impacts of heat flux and thermal conductivity on MHD-HNF flow in permeable media with slip conditions were discussed by Obalalu et al. [40]. As a result, they discovered that whereas in a squeezing condition, an increase in hybrid nanoparticle concentration improves the hybrid nanofluid's efficiency in heat transmission. Nadeem et al. [41] presented an analysis of stagnation point flow (SPF) and heat transmission characteristics of a second-grade MHD-HNF through a permeable medium under convective heating. Shah et al. [42] undertook an analysis of the thermal conductivity of a stable fly ash-Copper (40:10 vol%) and water-based fly ash nanofluids. The experimental measurements were conducted over a temperature range (30–60 °C), considering volume concentrations varying from 0 % to 4 %. Akhter et al. [43] scrutinized the energy conduction through a thermal stretchable sheet employing a Prandtl-Eyring nanofluid made of petroleum-based fluid. Automotive oil was used as a base fluid whereas TiO2 and Cu NPs were added to create the nanofluid. Ukan et al. [44] investigated the temperature and fluid flow features as well as entropy generation in a buoyant flow of HNF within a partly heated cavity occupied with porous material. Kumar et al. [45] explored the viscoelastic properties of a particular kind of HNF in an ambient temperature between 5.0 and 55 °C and various experimental environments. The outcomes of laboratory experiments, as well as flow and power-law curves, suggested that HNFs exhibited non-Newtonian behavior. The blood flow analysis inside different arteries using non-Newtonian Sisko model for application in biomedical engineering were study by Ref. [46]. The numerical investigation of non-Newtonian blood flow within an artery with cone shape of stenosis in various stenosis angles were study by Ref. [47]. The thermal behavior of blood flow in the arteries with various radii and various stenosis angles using non-Newtonian Sisko model were study by Ref. [48]. The roll of stenosis severity, artery radius and blood fluid behavior on the flow velocity in the arteries were study by Ref. [49]. Several research studies have been conducted to examine hybrid nanofluids (HNFs) (see Refs. [50–52]). Paul et al. [53] examine the demonstration of angioplasty using a balloon catheter in a tetra-hybrid nano-bloodstream within an electrified stenotic arterial cavity under a magnetic field. The exploring stream patterns of titania-CNTs blended blood in a squeezed artery subject to electro-magnetization, Hall and ion-slip currents were studied by Ref. [54]. A neural network approach to explore bioelectromagnetics aspects of blood circulation conveying tetra-hybrid nanoparticles and microbes in a ciliary artery with an endoscopy span was studied [55]. Applications of neuro-computing and fractional calculus to blood streaming conveying modified trihybrid nanoparticles with interfacial nanolayer aspect inside a diseased ciliated artery under electroosmotic and Lorentz forces were studied by Ref. [56]. EDL induced electro-magnetized modified hybrid nano-blood circulation in an endoscopic fatty charged arterial indented tract. was studied by Ref. [57]. The EDL-impelled flow of magnetized micropolar CNTs-Ingrained blood through a squeezed arterial channel was studied by Ref. [58]. EDL aspects in swirling ionic tribological fluid flow in a squeezed/split channel underlying a high-power magnetic field were studied by Ref. [59]. Simulation of magneto-nano-bioconvective coating flow with blowing and multiple slip effects was studied by Ref. [60]. Nano-bioconvective anisotropic slip flow in an anisotropic porous medium with Coriolis force effects was studied by Ref. [61]. Bio-nano convective micropolar fluid flow in a darcy porous medium past a cone with second-order slips and Stefan blowing was studied by Ref. [62]. Hamad et al. [63] Investigate the combined heat and mass transfer by Lie group analysis with variable diffusivity taking into account hydrodynamic slip and thermal convective boundary conditions. Three-dimensional bioconvection nanofluid flow from a bi-axial stretching sheet with anisotropic slip was studied by Ref. [64]. Multiple slips and variable transport property effects on magnetohydrodynamic dissipative thermosolutal convection in a porous medium were studied [65]. The computation of rheological nanofluid coating boundary layer transport with convective wall heating was studied by Refs. [66,67]. A two-layered suspension (particle-fluid) model for non-Newtonian fluid flow in a catheterized arterial stenosis with slip condition at the wall of a stenosed artery was studied [68]. The electroosmotic effect on two immiscible (conducting–non-conducting) fluids flowing in the porous channel under a magnetic field was studied by Ref. [69]. Effects of magnetic force and non-Newtonian characteristics on squeeze film bearings were studied by Ref. [70]. Particulate suspension Jeffrey fluid flow in a stenosed artery with a particle-free plasma layer near the wall was studied by Ref. [71].

1.1. Novelty of the newly proposed model

The present research addresses significant gaps in previous studies, which primarily focused on the modeling of blood flow through a squeezed arterial channel. Remarkably, previous works neglected the significance of the electric double layer and microrotation of blood particles, which are now thoroughly explored in this present research. This analysis aims to understand the influence of these combined effects on the flow behavior, microrotation bio-physical entities, entropy generation temperature, and mass concentration within the squeezed arterial channel. The electric double-layer effect is investigated to estimate and enhance blood flow systems, which is essential for improving the performance of electrochemical sensors used in blood analysis. The comparative investigation of *CuO*-MoS_2 - Cu/Blood tri-hybrid nanofluid and *CuO*-MoS_2 /Blood hybrid nanofluid is considered. The analysis examines the blood flow behavior of magnetized micropolar, focusing on factors such as non-linear thermal radiation, Helmholtz-Smoluchowski velocity, and vortex viscosity to gain a deeper understanding of their effects on blood flow dynamics. The non-linear ODEs with boundary conditions are solved through numerical methods using the finite element method with the assistance of MATHEMATICA 11.3 software.

1.2. Applications

The research of blood flow dynamics in the existence of external magnetic fields has gained substantial attention due to its prospective applications in medical treatments, such as heart disease, liver problems, and hypertension. Furthermore, the inclusion of molybdenum disulfide (MoS_2), copper oxide (CuO), and copper (Cu), as nanostructured materials in the blood can increase their thermal and electrical conductivity. This enhancement will provide significant benefits in medical technologies, such as controlling blood temperature during treatments and monitoring heart function. The application of copper (Cu), molybdenum disulfide (MoS_2), copper oxide (CuO), is displayed

in Fig. 1a-c respectively.

2. Mathematical background of the problem

We analyze a two-dimensional flow of rotational motion of blood particles within a compressing arterial channel, incorporating copper (Cu), molybdenum disulfide (MoS_2), copper oxide (CuO), nanomaterial. A diagram illustrating the flow configuration is provided in Fig. 1d. The following assumptions form the basis of the proposed model.

- The distance between the artery walls is defined by $h(t) = l\sqrt{1-at}$, with the condition that is $t < 1$, where t and a are time and a key parameter, respectively.
- At $= 1/a$, the upper wall comes into contact with the lower wall, having been initially positioned at $y = l$ when $t = 0$.
- When a is negative, the walls of the channel are positioned to create a separating effect, but when a is positive, the arterial walls compress the flow.
- In this setup, the orthogonal direction is the $\tilde{y}$-axis, and the horizontal direction is denoted by the $\tilde{x}$-axis, with the flow occurring within the $\tilde{x}\tilde{y}$-plane.
- Thermal transport analysis of the blood dynamical model has been carried out with the inclusion of thermal and concentration slip conditions.
- The transient velocity $v_h = dh/dt$ describes the squeezing motion of the upper wall.

2.1. Electric double layer (EDL) computation

When a surface is submerged in an electrolyte solution (ES), the electrified surface influences the ions within the solution, resulting in the attraction or repulsion of these ions. This interaction leads to the formation of a layer of ions with opposite charges situated near the surface, while ions with the same charge are pushed further away. This leads to the creation of an EDL. Furthermore, the Poisson-Boltzmann equation plays an important function in the fields of electrostatics, physical chemistry, electrochemical systems, and nanotechnology. At the interface between an ES and the EDL, this process is typically used to describe the EDL's formation. The electric potential resulting from the creation of an electrical double layer is expressed through the Poisson-Boltzmann expression as follows:

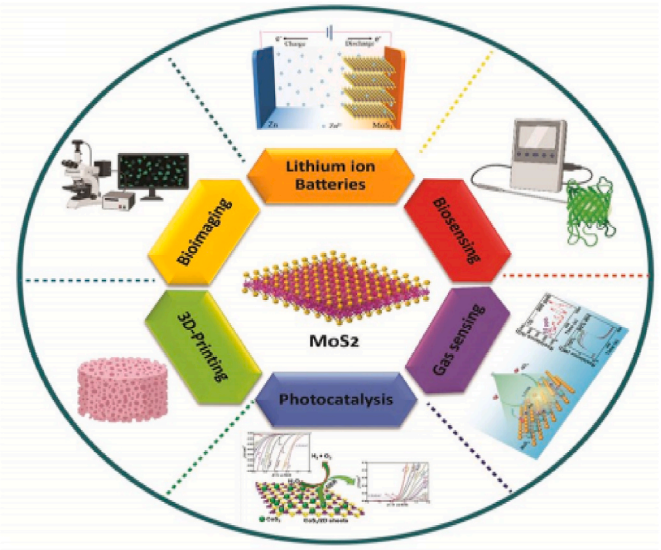


Fig. 1b. Applications of molybdenum disulfide nanoparticle.

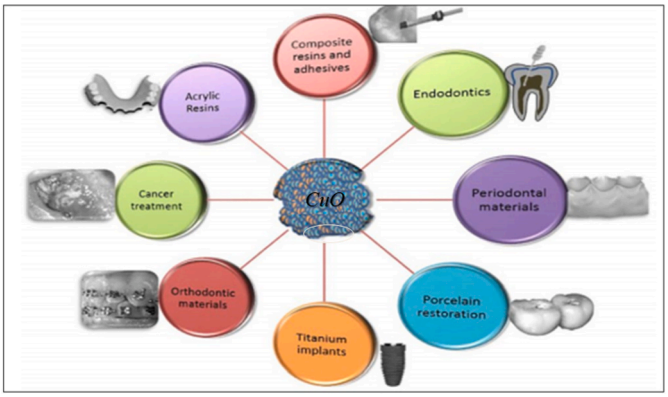


Fig. 1c. Applications of copper oxide nanoparticle.

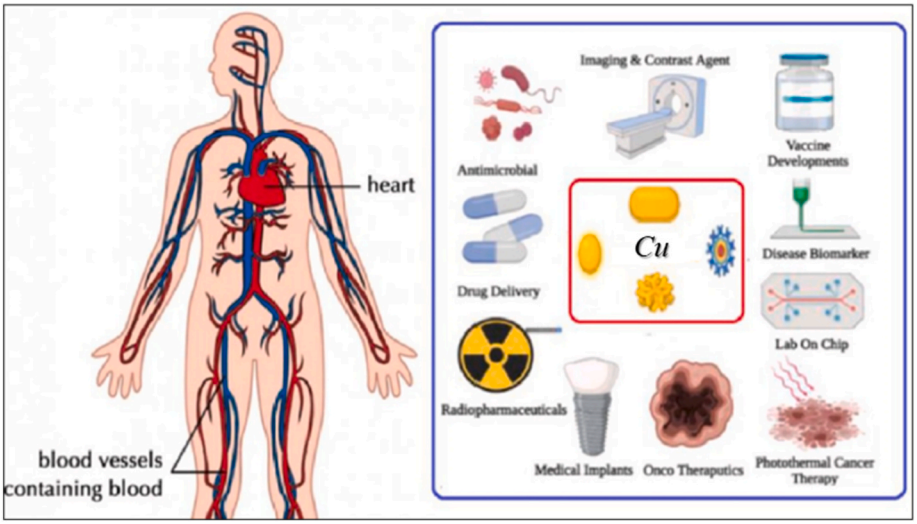


Fig. 1a. Applications of coppernanoparticles.

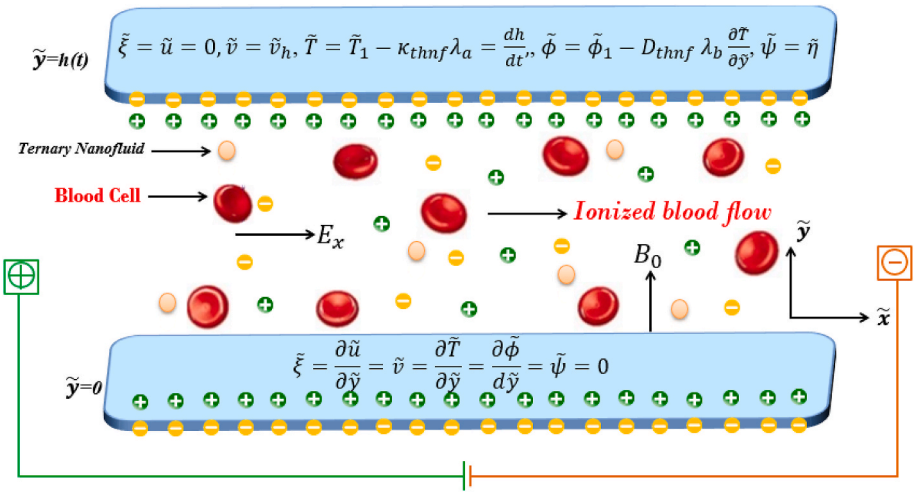


Fig. 1d. Geometry of the flow problem.

$$\frac{\partial^2 \tilde{\psi}}{\partial \tilde{x}^2} + \frac{\partial^2 \tilde{\psi}}{\partial \tilde{y}^2} = -\frac{\tau_r}{\varepsilon_{rf}}. \tag{1}$$

Here τ_r , ε_{rf} are the net ionic charge density and dielectric constant, respectively. Assuming that the cations and anions have the same valence C_w, the balanced ionic composition of the blood is calculated, as illustrated below:

$$\tau_r = rC_w(n^+ - n^-), \tag{2}$$

$$n_{\pm} = n_0 \exp\left(\mp \frac{rC_w\tilde{\psi}}{k_D T_C}\right). \tag{3}$$

In this context, number densities of cations and anions are represented as ($n^+$and n^-)average temperature (T_C), electron charge (r), bulk ionic concentration (n_0), ionic valence within the blood (E_w), the Boltzmann constant k_D. By replacing equations (2) and (3) with equation (1), the Poisson Boltzmann expression in the EDL is obtained as:

$$\frac{\partial^2 \tilde{\psi}}{\partial \tilde{x}^2} + \frac{\partial^2 \tilde{\psi}}{\partial \tilde{y}^2} = \frac{2rC_w n_0}{\varepsilon_{rf}} \sinh\left(\frac{rE_w\tilde{\psi}}{k_D T_C}\right). \tag{4}$$

2.2. Governing equations

The rotational motion of the blood particles and electric double layer (EDL) flow containing molybdenum disulfide (MoS_2), copper oxide (CuO), copper (Cu) ternary nanofluid are formulated as follows [36]:

$$\rho_{thnf}\left(\frac{\partial \tilde{u}}{\partial t} + \tilde{u}\frac{\partial \tilde{u}}{\partial \tilde{x}} + \tilde{v}\frac{\partial \tilde{u}}{\partial \tilde{y}}\right) = -\frac{\partial P}{\partial \tilde{x}} + \left(\mu_{thnf} + k_a\right)\left(\frac{\partial^2 \tilde{u}}{\partial \tilde{x}^2} + \frac{\partial^2 \tilde{u}}{\partial \tilde{y}^2}\right) + k_a\frac{\partial \tilde{\xi}}{\partial \tilde{y}} - \sigma_{thnf}B_0^2\tilde{u} + \tau_r E_x \tag{5}$$

$$\rho_{thnf}\left(\frac{\partial \tilde{v}}{\partial t} + \tilde{u}\frac{\partial \tilde{v}}{\partial \tilde{x}} + \tilde{v}\frac{\partial \tilde{v}}{\partial \tilde{y}}\right) = -\frac{\partial P}{\partial \tilde{y}} + \left(\mu_{thnf} + k_a\right)\left(\frac{\partial^2 \tilde{v}}{\partial \tilde{x}^2} + \frac{\partial^2 \tilde{v}}{\partial \tilde{y}^2}\right) - k_a\frac{\partial \tilde{\xi}}{\partial \tilde{x}} - \sigma_{thnf}B_0^2 v, \tag{6}$$

$$\rho_{thnf}j^*\left(\frac{\partial \tilde{\xi}}{\partial t} + \tilde{u}\frac{\partial \tilde{\xi}}{\partial \tilde{x}} + \tilde{v}\frac{\partial \tilde{\xi}}{\partial \tilde{y}}\right) = -2k_1\tilde{\xi} + k_a\left(\frac{\partial \tilde{v}}{\partial \tilde{x}} - \frac{\partial \tilde{u}}{\partial \tilde{y}}\right) + \left(\mu_{thnf}j + \frac{k_a j^*}{2}\right)\left(\frac{\partial^2 \tilde{\xi}}{\partial \tilde{x}^2} + \frac{\partial^2 \tilde{\xi}}{\partial \tilde{y}^2}\right) \tag{7}$$

$$\begin{aligned}(\rho c_p)_{thnf}\left(\frac{\partial \tilde{T}}{\partial t} + \tilde{u}\frac{\partial \tilde{T}}{\partial \tilde{x}} + \tilde{v}\frac{\partial \tilde{T}}{\partial \tilde{y}}\right) &= \kappa_{thnf}\left(\frac{\partial^2 \tilde{T}}{\partial \tilde{x}^2} + \frac{\partial^2 \tilde{T}}{\partial \tilde{y}^2}\right) + 4\mu_{thnf}\left(\frac{\partial \tilde{v}}{\partial \tilde{y}}\right)^2 \\ &+ \mu_{thnf}\left(\frac{\partial \tilde{u}}{\partial \tilde{y}} + \frac{\partial \tilde{v}}{\partial \tilde{x}}\right)^2 + \frac{k_a}{2}\left(\frac{\partial \tilde{v}}{\partial \tilde{x}} - \frac{\partial \tilde{u}}{\partial \tilde{y}} - 2\tilde{\xi}\right)^2 \\ &+ Q_0\tilde{\phi} + \left(\mu_{thnf}j^* + \frac{k_a j^*}{2}\right)\left[\left(\frac{\partial \tilde{\xi}}{\partial \tilde{x}}\right)^2\right. \\ &\left.+ \left(\frac{\partial \tilde{\xi}}{\partial \tilde{y}}\right)^2\right] - \frac{\partial q_r}{\partial \tilde{y}} + \sigma_{thnf}B_0^2(\tilde{u}^2 + \tilde{v}^2) \\ &+ \sigma_{thnf}E_x^2,\end{aligned} \tag{8}$$

$$\frac{\partial \tilde{\phi}}{\partial t} + \tilde{u}\frac{\partial \tilde{\phi}}{\partial \tilde{x}} + \tilde{v}\frac{\partial \tilde{\phi}}{\partial \tilde{y}} = D_{thnf}\left(\frac{\partial^2 \tilde{\phi}}{\partial \tilde{x}^2} + \frac{\partial^2 \tilde{\phi}}{\partial \tilde{y}^2}\right) - k_r^2\tilde{\phi}\left(\frac{\tilde{T}}{\tilde{T}_1}\right)^n e^{-\frac{E_a}{\kappa_B}}, \tag{9}$$

Subjected to Ref. [24]:

$$\begin{aligned}\tilde{\xi} = 0, \frac{\partial \tilde{u}}{\partial \tilde{y}} = 0, \tilde{v} = 0, \frac{\partial \tilde{T}}{\partial \tilde{y}} = 0, \frac{\partial \tilde{\phi}}{\partial \tilde{y}} = 0, \tilde{\psi} = 0 \text{ at } \tilde{y} = 0, \tilde{\xi} = 0, \tilde{u} = 0, \tilde{v} = \tilde{v}_h \\ = \frac{dh}{dt}, \tilde{T} = \tilde{T}_1 - \kappa_{thnf}\lambda_a\frac{\partial \tilde{T}}{\partial \tilde{y}}, \tilde{\phi} = \tilde{\phi}_1 - D_{thnf}\,\lambda_b\frac{\partial \tilde{\phi}}{\partial \tilde{y}}, \tilde{\psi} = \tilde{\eta} \text{ at } \tilde{y} = h(t),\end{aligned} \tag{10}$$

In the governing equation, Table 1 shows the symbols and their corresponding descriptions.

2.3. Mathematical relations for thermophysical properties

Ternary nanofluids are advanced fluid systems consisting of three different types of nanoparticles suspended in a basefluid, typically a liquid like water, oil, or ethylene glycol. The unique feature of ternary nanofluids is the combination of multiple nanoparticle types, which may enhance thermal conductivity, heat transfer, and other thermophysical properties beyond the capabilities of binary or single-particle nanofluids. The thermophysical properties of the ternary nanofluids are provided as follows [35]:

Base fluid: Blood
Nanoparticles: $\vartheta_1 = \vartheta_{Cu}, \vartheta_2 = \vartheta_{CuO}, \vartheta_3 = \vartheta_{MoS_2}$,
$\vartheta_{nf} = \vartheta_1$
$\vartheta_{hnf} = \vartheta_1 + \vartheta_2$
$\vartheta_{thnf} = \vartheta_1 + \vartheta_2 + \vartheta_3$

(continued on next page)

Table 1
Symbols and description.

Symbols	Meaning of Symbols	Units	Symbols	Meaning of Symbols	Units
x,y	Velocity components	m/s	Q_0	Internal heat source coefficient	W/m^3
$(\rho c_p)_{thnf}$	Chemical reaction coefficient	J/(kg·K)	C_r	Concentration slip length	m
ξ	Microrotation	rad/s	κ_{thnf}	Thermal conductivity	W/(m.k)
P	Pressure	$Pa(N/m^2)$	η	Zeta potential at the upper plate	V (volts)
λ_a	Thermal slip length	m	$\widetilde{T}$	Temperature	K (kelvin)
k_D	Boltzmann's constant	J/K	$\widetilde{\phi}$	Concentration	kg/m^3 or dimensionless
n	Fitted rate constant	Depends on reaction (e.g., s^{-1})	D_{thnf}	Mass diffusivity	m^2/s
j^*	Micro-inertia density	$kg{\cdot}m^2$	k_a	Micropolar viscosity	Pa.s ($N{\cdot}s/m^2$)
q_r	Radiative heat flux	W/m^2	E_a	Activation energy	J/mol
k*	absorption coefficient	m^{-1}	σ*	Stefan Boltzmann constant	$W{\cdot}m^2{\cdot}K^{-4}$

(*continued*)

Viscosity:

$$\frac{\mu_{nf}}{\mu_f}=\frac{1}{((1-\vartheta_{Cu}))^{2.5}},$$

$$\frac{\mu_{hnf}}{\mu_f}=\frac{\mu_f}{((1-\vartheta_{Cu})(1-\vartheta_{CuO}))^{2.5}},$$

$$\frac{\mu_{thnf}}{\mu_f}=\frac{\mu_f}{((1-\vartheta_{Cu})(1-\vartheta_{CuO})(1-\vartheta_{MoS_2}))^{2.5}},$$

Heat Capacity:

$$(\rho c_\rho)_{nf1}=(1-\vartheta_{Cu})+\frac{(\rho C_p)_1}{(\rho C_p)_f}\vartheta_{Cu},\frac{(\rho C_p)_{nf}}{(\rho C_p)_f}=(\rho c_\rho)_{nf1}$$

$$(\rho c_\rho)_{nf2}=(1-\vartheta_{CuO})+\frac{(\rho C_p)_2}{(\rho C_p)_f}\vartheta_{CuO},\frac{(\rho C_p)_{hnf}}{(\rho C_p)_f}=(\rho c_\rho)_{nf1}+(\rho c_\rho)_{nf2}$$

$$(\rho c_\rho)_{nf3}=(1-\vartheta_{MoS_2})+\frac{(\rho C_p)_3}{(\rho C_p)_f}\vartheta_{MoS_2},\frac{(\rho C_p)_{thnf}}{(\rho C_p)_f}=(\rho c_\rho)_{nf1}+(\rho c_\rho)_{nf2}+(\rho c_\rho)_{nf3}$$

Electrical Conductivity:

$$\sigma_{nf1}=\frac{(1+2\vartheta_{Cu})\sigma_1+(1+2\vartheta_{Cu})\sigma_{nf}}{(1+\vartheta_{Cu})\sigma_1+(1+2\vartheta_{Cu})\sigma_{nf}}\quad\frac{\sigma_{nf}}{\sigma_f}=\frac{(\sigma_{nf1}\vartheta_{Cu})}{\vartheta_{nf}}$$

$$\sigma_{nf2}=\frac{(1+2\vartheta_{CuO})\sigma_2+(1+2\vartheta_{CuO})\sigma_{hnf}}{(1+\vartheta_{CuO})\sigma_2+(1+\vartheta_{CuO})\sigma_{hnf}}\quad\frac{\sigma_{hnf}}{\sigma_f}=\frac{(\sigma_{nf1}\vartheta_{Cu}+\sigma_{nf2}\vartheta_{CuO})}{\vartheta_{hnf}}$$

$$\sigma_{nf3}=\frac{(1+2\vartheta_{MoS_2})\sigma_3+(1+2\vartheta_{MoS_2})\sigma_{thnf}}{(1+\vartheta_{MoS_2})\sigma_3+(1+\vartheta_{MoS_2})\sigma_{thnf}}\quad\frac{\sigma_{thnf}}{\sigma_f}=\frac{\left(\sigma_{nf1}\vartheta_{Cu}+\sigma_{nf2}\vartheta_{CuO}+\sigma_{nf3}\vartheta_{MoS_2}\right)}{\vartheta_{thnf}}$$

Thermal Conductivity: $k_{nf1}=\frac{(k_1+2k_f)-2\vartheta_{Cu}(k_f-k_1)}{(k_1+2k_f)+\vartheta_{Cu}(k_f-k_1)}\quad\frac{k_{nf}}{k_f}=\frac{(k_{nf1}\vartheta_{Cu})}{\vartheta_{nf}}$

$$k_{nf2}=\frac{(k_2+2k_{nf1})-2\vartheta_{CuO}(k_{nf}-k_2)}{(k_2+2k_{nf1})+\vartheta_{CuO}(k_{nf}-k_2)}\quad\frac{k_{hnf}}{k_f}=\frac{(k_{nf1}\vartheta_{Cu}+k_{nf2}\vartheta_{CuO})}{\vartheta_{hnf}}$$

$$k_{nf3}=\frac{(k_3+2k_{nf2})-2\vartheta_{MoS_2}(k_{nf2}-k_3)}{(k_3+2k_{nf2})+\vartheta_{MoS_2}(k_{nf2}-k_3)}\quad\frac{k_{thnf}}{k_f}=\frac{(k_{nf1}\vartheta_{Cu}+k_{nf2}\vartheta_{CuO}+k_{nf3}\vartheta_{MoS_2})}{\vartheta_{thnf}}$$

Density:

$$\frac{\rho_{nf}}{\rho_f}=(1-\vartheta_{Cu})+\vartheta_{Cu}\frac{\rho_1}{\rho_f}$$

$$\frac{\rho_{hnf}}{\rho_f}=(1-\vartheta_{Cu})\left[1-\vartheta_{Cu}\left\{(1-\vartheta_{CuO})+\vartheta_{CuO}\frac{\rho_2}{\rho_f}\right\}+\vartheta_{CuO}\frac{\rho_2}{\rho_f}\right]\vartheta_{Cu}\frac{\rho_1}{\rho_f}$$

$$\frac{\rho_{thnf}}{\rho_f}=(1-\vartheta_{Cu})\left[1-\vartheta_{CuO}\left\{(1-\vartheta_{MoS_2})+\vartheta_{CuO}\frac{\rho_2}{\rho_f}\right\}+\vartheta_{MoS_2}\frac{\rho_3}{\rho_f}\right]\vartheta_{Cu}\frac{\rho_1}{\rho_f}$$

Mass diffusivity:

$$D_{thnf}=D_f(1-\vartheta)$$

Thermal characteristics of *Cu*, *CuO*, MoS_2 and Blood base fluid are shown in Table 2 [36].

Table 2
Physical properties of (*Cu*, *CuO*, MoS_2) and the base fluid (Blood).

Physical property	$\rho(kg/m^3)$	C_p (J/kgK)	k (W/mK)	σ $(S\ m^{-1})$
Blood	1150	3617	0.53	0.7
Copper Oxide(*CuO*)	6500	533	17.65	$10^{-4}-10^{-2}$
MoS_2	5060	397.21	904.4	2.09×10^{-5}
Copper (*Cu*)	8933	385	400	5.96×10^{7}

The radiative heat flux (qr) with the guidance of Rosseland approximation [67] can be stated as:

$$q_r=-4\sigma^*3k^*\frac{\partial\widetilde{T}^4}{\partial y}=-\frac{16\sigma^*}{3k^*}\widetilde{T}^3\frac{\partial\widetilde{T}}{\partial y}. \tag{11}$$

2.4. Similarity transformations

Similarity transformations are mathematical techniques used to simplify partial differential equations (PDEs) or boundary value problems by reducing the number of independent variables. This is typically achieved by introducing similarity variables, which are combinations of the original variables that collapse multiple dimensions into a single dimension. In fluid dynamics and heat transfer problems, similarity transformations help convert complex PDEs into simpler ordinary differential equations (ODEs), making them easier to analyze or solve numerically. The similarity transformations are ([72,73,67]):

$$\widetilde{u}=\frac{a\widetilde{x}}{2(1-at)}f'(\chi),\beta=\frac{\widetilde{\phi}}{\widetilde{\phi}_1},P=\frac{\mu_f}{\widetilde{x}}\frac{a\widetilde{x}}{2(1-at)}p(\chi),\widetilde{v}=\frac{-al}{2\sqrt{1-at}}f(\chi),\varnothing=\frac{rC_w\widetilde{\psi}}{k_DT_C},\theta=\frac{\widetilde{T}-\widetilde{T}_0}{\widetilde{T}_1-\widetilde{T}_0},\widetilde{\xi}=\frac{a\widetilde{x}}{2l}(1-at)^{-\frac{3}{2}}g(\chi),\chi=\frac{\widetilde{y}}{h(t)}.. \tag{12}$$

The dimensionless forms of governing equations with associated boundary conditions take the following form:

$$2A_2S_qf'+A_2S_q\chi f''-R_vg'-(A_1+R_v)f'''+A_2S_q(f')^2-A_2S_qff''+A_3M^2f'=\frac{2f^2(1-at)^2}{\mu_fa\widetilde{x}}\left(-\frac{\partial P}{d\widetilde{x}}+\tau_rE_x\right), \tag{13}$$

$$A_2S_q\chi f'-R_vg+A_2S_qf+A_3M^2f-(A_1+R_v)f''-A_2S_qf'=\frac{2l(1-at)^{3/2}}{\mu_fa}\frac{\partial P}{\partial\widetilde{x}} \tag{14}$$

$$M_1\left(A_1+\frac{R_v}{2}\right)g''-R_vf''-2R_vg=S_qM_1A_23g+S_qM_1A_2\chi g''+S_qM_1A_2gf'-S_qM_1A_2fg', \tag{15}$$

$$\begin{aligned}3N_r(\theta_w-1)[(\theta_w-1)\theta+1]^2(\theta'')^2+\frac{1}{2}R_vP_rE_c\,(f''+2g)^2&=A_4S_qP_r\,(\chi-f)\theta'-\lambda_3J\\&-A_1P_rE_c\left(4\varpi^2f'^2+f''^2\right)\\&+A_3P_rE_cM^2f'^2-\xi_q\beta\\&-M_1P_rE_c\left(\lambda_1+\frac{R}{2}\right)\left(\varpi^2g^2+g'^2\right)\\&-\lambda_3P_rE_cM^2\varpi^2f'^2,\end{aligned} \tag{16}$$

$$\lambda_6\,\beta''+S_qS_c\,\beta'(f-\eta)-K_r\beta\theta^n e^{-E_a/\theta}=0. \tag{17}$$

The following result is obtained by taking the derivative of equation (14) with respect to $\widetilde{x}$

$$\frac{\partial^2 P}{\partial \widetilde{x}\partial \widetilde{y}} = 0. \tag{18}$$

Utilizing equation (18) and differentiating equation (13) with respect to $\widetilde{y}$, the following result is obtained

$$(A_1 + R_v)f^{IV} - A_2 S_q(3f'' + \chi f''' - ff'' + f'f') = A_3 M^2 f'' - R_v g'' - U_D \mathscr{K}^2 \phi'. \tag{19}$$

By applying Equation (12), the electrical potential equation can be derived as follows [72]:

$$\varnothing'' - \mathscr{K}^2 \sinh\varnothing = 0. \tag{20}$$

Reduced boundary conditions are:

$$\begin{aligned} f(0) = 0, f''(0) = 0, f(1) = 1, f(1) = 0, g(0) = 0, g(1) = 0, \theta'(0) \\ = 0, \theta(1) + A_s T_s\, \theta'(1) = 1, \beta'(0) = 0, \varnothing(0) \\ = 0, \beta(1) + A_6 C_s\, \beta'(1) = 1, \varnothing(1) = \eta.. \end{aligned} \tag{21}$$

The solution to the Poisson–Boltzmann expression (19), and the BCs (20), is determined using the linearization approximation of Debye-Hückel, which simplifies to ($\sinh \varnothing \approx \varnothing$). This solution is shown as follows [73]:

$$\varnothing = \frac{\eta \sinh m\forall}{\sinh m}. \tag{22}$$

2.5. Parameter expression

The symbol S_q, ϖ, $E_a, R_v, \theta_w, K, M_1, \mathfrak{E}_q, P_r, \mathrm{K}_r, \mathscr{K}, U_{hs}, \mathrm{B}_r, M, N_r, C_s, U_D, J, x_1$ corresponds to the squeezing parameter, dimensionless axial variable, temperature ratio parameter, activation energy, Vortex viscosity, Debey-Hückel parameter, Micropolar parameter, Heat source parameter, Prandtl number, Chemical reaction, Electroosmosis parameter, Helmholtz-Smoluchowski velocity, Brinkman number, Hartmann number, Radiation Parameter, Concentration slip parameter, Electrical field parameter, Thermal slip parameter, Schmidt number, Joule heating parameter, Diffusion parameter.

$$S_q = \frac{a_{p_b}\rho^2}{2\mu_b}, \varpi = \frac{i\sqrt{1-at}}{\widetilde{x}}, E_a = \frac{E_1}{k_B T_1}, R_v = \frac{k_1}{\mu_0}, \theta_w = \frac{\widetilde{T}_1}{\widetilde{T}_0},$$

$$K = \left(\frac{2J_g^2 e^2 m_0}{\sigma_{ef} k_n T_H}\right)^{\frac{1}{2}}, M_1 = \frac{j^*}{l(1-at)}, \mathfrak{E}_q = \frac{Q_0 C_1 l^2 (1-ar)}{T_1 \kappa_b}, P_r = \frac{\mu_d(c_p)b}{\sigma_0}, \mathrm{K}_r = \frac{c_r^2 P^2 (1-at)}{D_b},$$

$$\mathscr{K} = Kl(1-at), U_{hs} = -\frac{2k_a T_\mu \varepsilon_\varepsilon E_x}{\mu_k z_c e}, Br = \frac{a^2 x^2 \mu_b}{4T_1 x_b (1-\alpha)^2}, M = hB_0\left(\frac{\sigma_g}{\mu_0}\right)^{1/2},$$

$$N_r = \frac{16\sigma^* T_0^3}{3\kappa_f k^*}, C_s = \frac{\gamma_2 \nu_0}{l\sqrt{1-at}}, U_D = \frac{1}{ax} U_{hs}, T_s = \frac{\gamma_1 k_b}{I\sqrt{1-at}}, S_c = \frac{\nu_a}{D_b}$$

$$J = \frac{\sigma_b E_a^2 P^2 (1-at)}{T_1 \kappa_b}, p_1 = \frac{\overline{R} D_s \phi_1}{\kappa_s}.$$

Also.

$\mathrm{A}_1 = \frac{\mu_{thnf}}{\mu_f}, \mathrm{A}_2 \frac{\rho_f}{\rho_{thnf}}$, $\mathrm{A}_3 = \frac{\sigma_{thnf}}{\sigma_f}, \mathrm{A}_4 = \frac{(\rho C_p)_{thnf}}{(\rho C_p)_f}, \mathrm{A}_5 = \frac{k_{thnf}}{k_f}$, $\mathrm{A}_6 = (1-\vartheta)$ are distinct nanoparticle concentrations.

In a dimensionless form, the drag coefficient, dimensionless temperature gradient, and dimensionless concentration gradient at the upper and lower walls of the channel are mathematically defined as:

$$C_f = \frac{\tau_w}{\rho_f u_w^2}, \text{where } \tau_w = \mu_{thnf}\left(\frac{\partial u}{\partial y}\right)_{y=\begin{cases} 0 \\ h(t) \end{cases}} \text{is the wall shear stress}$$

$$Nu_x = \frac{lq_w}{\kappa_f T_1}, \text{where } q_w = \left[-\kappa_{thnf}\left(\frac{\partial T}{\partial y}\right) + q_r\right]_{y=\begin{pmatrix} 0 \\ h(t) \end{pmatrix}} \text{is the wall heat flux}$$

and

$$Sh_x = \frac{lq_m}{D_f C_1}, \text{where } q_m = -D_{thnf}\left(\frac{\partial C}{\partial y}\right)_{y=\begin{cases} 0 \\ h(t) \end{cases}} \text{is the concentration flux.} \tag{23}$$

Then, the dimensionless of C_f, Nu_x,Sh_x are derived as:

$$R_{ex} Cf_{\text{upper}} \frac{l^2}{x^2}(1-at) = \frac{A_1}{A_2} f''(1), R_{\text{ex}}\, Cf_{\text{lower}} \frac{l^2}{x^2}(1-at)$$

$$= \frac{A_1}{A_2} f''(0), Nu_{\text{upper}}\,(1-at)^{1/2} = -\left(A_5 + N_r[(\theta_w - 1)\theta(1)\right.$$

$$\left.+1]^3\right)\theta'(1), Nu_{\text{lower}}\,(1-at)^{1/2} = -\left(A_5 + N_r[(\theta_w - 1)\theta(0)\right.$$

$$\left.+1]^3\right)\theta'(0), Sh_{\text{upper}}\,(1-at)^{1/2} = -A_6\beta'(1), Sh_{\text{lower}}\,(1-at)^{\frac{1}{2}} = -A_6\beta'(0).. \tag{24}$$

The dimensionless quantities are essential for describing the flow and the heat and mass transfer characteristics of blood as it moves through the arterial channel. They offer an efficient method for evaluating the comparative impacts of different factors and can be utilized to achieve a better understanding of the dynamics of nano-blood flow through the arterial channel.

3. Entropy generation analysis

The volumetric entropy generation rate in relation to the current blood flow situation can be defined mathematically as:

$$\begin{aligned} N_G = {} & \frac{\kappa_f}{\widetilde{T}_1^2}\left(\frac{\kappa_{thnf}}{\kappa_f} + \frac{16\sigma^* \widetilde{T}^3}{3\kappa_f k^*}\right)\left(\frac{\partial \widetilde{T}}{\partial \widetilde{y}}\right)^2 + \frac{1}{\widetilde{T}_1}\left(\mu_{thnf} j + \frac{k_1 J^*}{2}\right)\left[\left(\frac{\partial \widetilde{\xi}}{\partial \widetilde{x}}\right)^2\right. \\ & \left. + \left(\frac{\partial \widetilde{\xi}}{\partial \widetilde{y}}\right)^2\right] + \frac{k_1}{2\widetilde{T}_1}\left(\frac{\partial \widetilde{v}}{\partial \widetilde{x}} - \frac{\partial \widetilde{u}}{\partial \widetilde{y}} - 2\widetilde{\xi}\right)^2 + \frac{\sigma_{thnf} B_0^2}{\widetilde{T}_1}(\widetilde{u}^2 + \widetilde{v}^2) + \frac{\sigma_{thnf}}{\widetilde{T}_1} E_x^2 \\ & + \frac{4\mu_{thnf}}{\widetilde{T}_1}\left(\frac{\partial \widetilde{v}}{\partial \widetilde{y}}\right)^2 + \frac{\mu_{thnf}}{\widetilde{T}_1}\left(\frac{\partial \widetilde{v}}{\partial \widetilde{y}} + \frac{\partial \widetilde{v}}{\partial \widetilde{x}}\right)^2 + \frac{\widetilde{R} D_{thnf}}{T_1}\left(\frac{\partial \widetilde{\phi}}{\partial \widetilde{x}}\frac{\partial \widetilde{T}}{\partial \widetilde{x}} + \frac{\partial \widetilde{\phi}}{\partial \widetilde{y}}\frac{\partial \widetilde{T}}{\partial \widetilde{y}}\right) \\ & + \frac{\widetilde{R} D_{thnf}}{\widetilde{\phi}_1}\left[\left(\frac{\partial \widetilde{\phi}}{\partial \widetilde{x}}\right)^2 + \left(\frac{\partial \widetilde{\phi}}{\partial \widetilde{y}}\right)^2\right] \end{aligned} \tag{25}$$

3.1. Irreversibility analysis

In a dimensionless form, the rate of entropy production is

$$Gc = \frac{P_G}{P_C} = \frac{\rho^2 (1-at)}{\kappa_b} P_C. \tag{26}$$

When equation (12) and equation (25) are used in above equation, we get:

$$Gc = \left(A_5 + N_r[(\theta_w - 1)\theta + 1]^3\right)\theta'^2 + Brp_1\left(A_1 + \frac{\pi}{2}\right)\left(p_1{}^2 g^2 + g'^2\right) + \frac{k}{\Delta r}(f'' + 2g)^2 + A_1 Br\left(4\,\varpi^2 f''^2 + f''^2\right) + A_3 M^2 Br\left(\varpi^2 f^2 + f'^2\right) + \lambda_6 p_1\left(\beta'\theta' + \beta'^2\right) + A_3 J \quad (27)$$

4. Numerical solution

4.1. Application of finite element method

The Finite Element Method (FEM) is a numerical technique used to solve partial differential equations (PDEs) and integral equations. FEM is widely applied in engineering, physics, and computational fluid dynamics for modeling complex structures, materials, and systems. The method involves discretizing a domain into smaller subdomains called finite elements, over which the governing equations are approximated using interpolation functions. The solution is then assembled to approximate the behavior of the entire domain.

First **step:** Domain discretization is the process of dividing a complex, continuous domain into smaller, simpler, and finite subdomains called elements. This step transforms a problem defined over an infinite number of points into one defined over a finite number of points, which can be solved numerically.

Second step: Shape functions, also known as basis functions or interpolation functions, are mathematical functions used to approximate the solution of the governing equations within each element. They describe how the solution varies across an element and ensure continuity between adjacent elements.

Third step: The weak formulation is a mathematical approach that reformulates the governing partial differential equations (PDEs) into an integral form. This makes the equations easier to solve numerically, especially when using the finite element method (FEM). The weak formulation reduces the differentiability requirements for the solution and allows the inclusion of boundary conditions naturally.

Fourth step: The Generalized Finite Element Method (GFEM) extends the traditional FEM by introducing enrichment functions to improve solution accuracy without refining the mesh. These enrichment functions account for known physical features like singularities, discontinuities, or other complex behaviors in the solution.

Fifth step: The element equations are combined to form a global system of equations that models the entire problem domain. This system of algebraic equations is then solved numerically to obtain an approximate solution. Given the previously mentioned insufficient conditions, computations will be performed with a precision of 10^{-5}, ensuring a high level of computational accuracy where $\left|\frac{\wp^{i+1}-\wp^{i}}{\wp^{i+1}}\right| < 10^{-5}$.

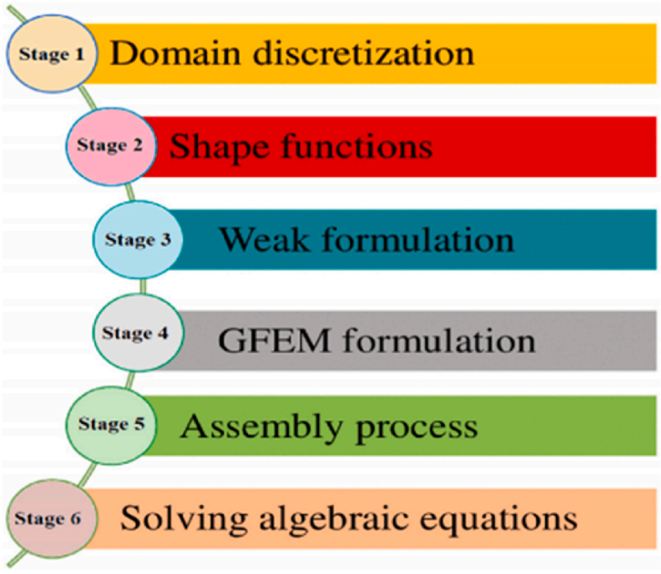


Fig. 1e. Step-by-step process for the Finite Element Method (FEM).

Sixth step: In step 6 of the Finite Element Method, the global system of algebraic equations is solved, typically using numerical methods, to compute the while incorporating boundary conditions to ensure the solution accurately reflects the physical problem. Fig. 1e display the Step-by-step process for the Finite Element Method (FEM).

4.2. Validity of the results

As the results show a reasonable agreement between the current and previous findings, the current numerical code is validated (see Table 3). A comparison with previously published results (Refs [72,73]) is provided in Table 2, where the results are in perfect agreement.

5. Results and discussion

This article investigates micropolar blood flow in squeezed arterial channels under the influence of a magnetized ternary nanofluid and an electric double layer. The heat transfer characteristics of the flow through an arterial squeezed channel are analyzed and illustrated using figures and tables. The variation in these quantities has been computed for appropriate ranges of significant parameters. Table 4 demonstrates the rate of thermal energy through computational processes.

5.1. Velocity

Hartmann number (M) parameter: Fig. 2a shows the influences of varying Hartmann number (M). A comparison is made between *CuO*-MoS_2 - Cu/Blood tri-hybrid nanofluid and *CuO*-MoS_2 /Blood hybrid nanofluid. As the values of M increase, the primary speed in the lower section of the squeezed arterial channel decreases. This reveals that stronger magnetic field strength produces a substantial obstruction to the fluid flow. On the contrary, in the upper region of the squeezed arterial channel, the flow performance exhibits a greater achievement of velocity flow. In MHD applications, the Hartmann number determines the extent to which the flow of an electrically conducting fluid (like liquid metals or plasmas) is influenced by an external magnetic field. This is crucial in nuclear reactors, where liquid metal coolants are used. The expression A_3M^2f' equation (12) represents the Lorentz drag force, which exerts an increasing influence in both the lower and upper sections of the arterial channel. The speed flow of the *CuO*-MoS_2 - Cu/Blood tri-hybrid nanofluid is notably higher than that of the *CuO*-MoS_2 /Blood hybrid nanofluid in the lower and upper regions of the arterial channel. Furthermore, no backflow is observed throughout the channel gap. Physically, the utilization of a magnetic field can result in vaso-relaxation, which refers to the narrowing (constriction) of blood vessels. This constriction upsurges the resistance of the blood flow and reduces the flow movement of blood throughout the arterial channel.

Electrical field parameter (U_D): The U_D parameter is a characteristic that illustrates the performance of an electric field (EF) in various systems. An EF is a force field that occurs around particles with electric charge. The effect of U_D parameter on $f'(\chi)$ is displayed in Fig. 2b. The diagram demonstrates that the primary flow increases with ithe ncreasing value of U_D parameter. In graph, it is noted that the $f'(\chi)$ of *CuO*-MoS_2 - Cu/Blood tri -hybrid nanofluid is greater than

Table 3
Numerical comparison results for Nu_x.

S_q	−1.0	−0.5	0.01	0.5	2.0
Outcome of [72]	2.17015	2.61742	3.00713	3.33644	4.16740
Outcome of [73]	2.17009	2.61740	3.00713	3.33645	4.16739
Present result	2.17015	2.61742	3.00713	3.33644	4.16740

Table 4
Computed values of Nu_x.

Parameter	Values	Nu_x	Heat transport rate influence
M	**0.1**	**4.41519**	An increase in the Nusselt number occurs as a result of more efficient thermal transport from the arterial wall to the blood. This improvement is attributed to stronger magnetic forces that align the blood flow with these forces. As the M parameter increases, these magnetic influences become more significant.
	0.2	**4.53872**	
	0.3	**4.65563**	
N_r	**0.3**	**4.67023**	As the value of N_r raises, radiative thermal transport becomes more substantial relative to conductive thermal transport in blood flow. Due to the increased loss of heat through radiation, the amount of heat that is transferred convectively from the arterial wall to the blood is reduced, leading to this reduction. Therefore, the convective thermal transport coefficient reduces, leading to a decline in the Nu_x.
	0.2	**4.65563**	
	0.3	**4.52392**	
J	**0.1**	**4.5806**	The Nu_x increases as a result of an enhanced rate of thermal transport from the blood to the arterial wall. This enhancement is achieved through increased temperature differences near the wall, which arise from a rise in the blood's temperature. As the *J* parameter increases, resistive heating becomes more intense, resulting in more electrical energy being converted into heat within the blood, which causes this temperature rise.
	0.2	**4.62911**	
	0.4	**4.71935**	
T_s	**0.1**	**4.57092**	The Nu_x decreases due to a reduced transport of heat from the blood to the wall, resulting in less heat being transported.
	0.2	**4.43725**	
	0.3	**4.38399**	

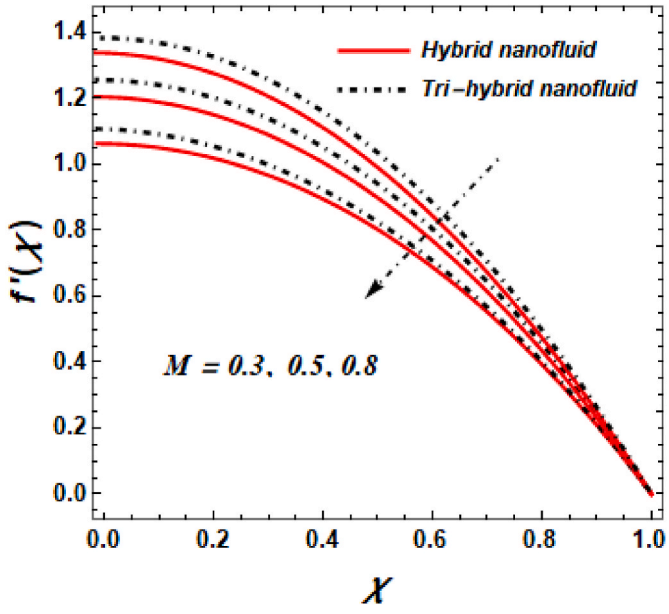


Fig. 2a. Impact of M on f′(χ).

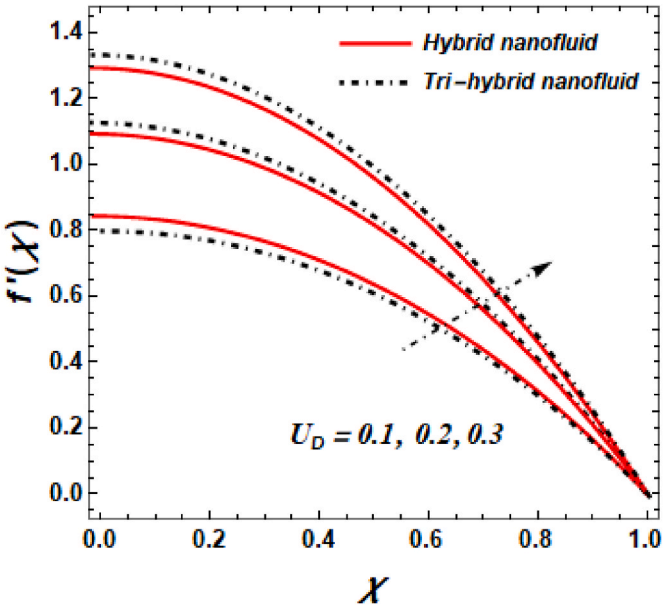


Fig. 2b. Impact of U_D on f′(χ).

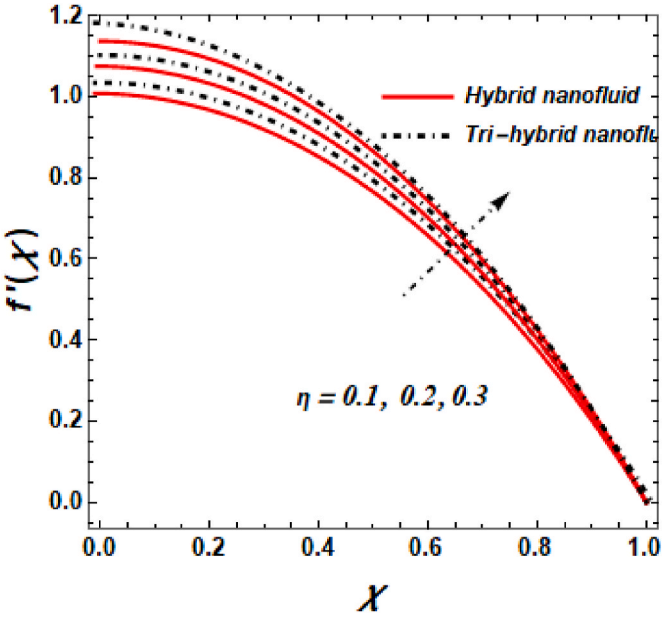


Fig. 2c. Influence of η on f′(χ).

CuO-MoS_2 /Blood hybrid nanofluid. As the U_D parameter elevated, the key physical justification for the rise in blood flow is the intensified movement of ions present in the blood [51]. The forces produced via this movement, which is inspired by the EF, contribute to pushing the blood forward. This action reduces resistance and increases the momentum of blood flow. The electrical field parameter related to blood flow is crucial in analyzing the behavior of blood (a weakly conducting fluid due to its ionic content) under the influence of an external or induced electric field.

Zeta potential parameter (η) parameter: Fig. 2c explains the effect of the (η) parameter variable for both *CuO*-MoS_2 -Cu/Blood tri-hybrid nanofluid and *CuO*-MoS_2 /Blood hybrid nanofluid on fluid motion. This η parameter relates to the boundary condition at the upper wall, expressed as $\Phi(1) = \eta$. High values of η parameter have a considerable outcome on the electro-osmotic flow of blood, whereas lesser values of η parameters result in slight changes the f′(χ). The applied electric field influences the process by which the cations present in the ionic blood are attracted toward the anions located on the inner surfaces of the arterial walls, resulting in the formation of a positive charge density within the electric double layer. This charge density reduces quickly as the distance from the arterial walls rises [52]. The zeta potential (η) parameter is described as the voltage difference that occurs close to the wall. As the value η improved, cations felt a pull toward the cathode due to an attractive force. Therefore, this increases the electrokinetic blood circulation. The *CuO*-MoS_2 - Cu/Blood tri-hybrid nanofluid demonstrates more fascinating speed than *CuO*-MoS_2 /Blood hybrid nanofluid within

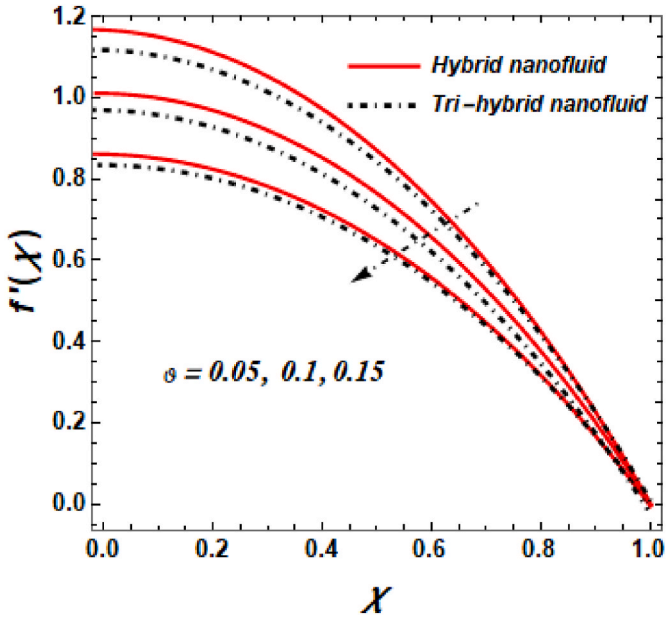


Fig. 2d. Effect of ϑ on $f'(\chi)$.

the upper and lower regions of the arterial channel. The zeta potential plays a significant role in determining the aggregation and dispersion of RBCs, which directly affects blood viscosity. A high zeta potential (more negative charge) promotes cell repulsion and smooth blood flow, while a low zeta potential can lead to RBC aggregation, increasing viscosity and potentially causing clotting.

The dimensionless volume fraction of nanoparticles (ϑ): Fig. 2d shows how the ϑ affects the movement of liquid in both tri-hybrid nanofluid and hybrid nanofluid. The Curves in Fig. 2d show a downward trend in the $f'(\chi)$. This shows that as the value ϑ rises, the $f'(\chi)$ at which the liquid moves diminishes. In reality, the addition of nanoparticles to a fluid can boost its viscosity. A fluid that has a higher viscosity will demonstrate a slower flow compared to one with a lower viscosity.

5.1.1. Temperature

Thermal radiation (Nr): The impact of the thermal radiation parameter along the heat propagation has been revealed in Fig. 3a. As the Nr parameter upsurges, it reduces the blood temperature in the vascular system. The thermal boundary thickness decreases as thermal radiation increases when the system is confined between two arterial channel walls, as demonstrated by the current simulation. Also, the heat propagation of the blood reduces as a result of heat loss. This heat loss occurs because, with a higher Nr, the circulatory system permits a larger amount of Nr to be emitted from the ingrained blood. DNA of cancer cells in internal radiation therapy can benefit from this study. Similar observations have been study via [72].

Joule heating (J) parameter: Fig. 3b displays the effect of the J parameter on the thermal profile. It is seen that an increase in the value of the joule heating J parameter results in a rise in the heat propagation of the bloodstream. Joule heating refers to the phenomenon where the flow of electric current (EC) through a conductor generates heat. When an electric current flows through the bloodstream, the blood's resistance produces heat. As Joule heating characterizes the amount of electrostatic energy converted into heat, more heat production occurs within the bloodstream. However, the inspiration of *CuO*-MoS_2 - Cu/Blood tri-hybrid nanofluid is more prominent than the *CuO*-MoS_2 /Blood hybrid nanofluid.

Electroosmosis parameter ($\mathscr{H}$): These curves in Fig. 3c show a dimensionless rate of heat propagation plotted against the electroosmosis parameter. As the values of the electroosmosis parameter upsurge, the heat propagation shows a decrease. The physical reason for this phenomenon is that the current density of the bloodstream increases while the width of the electrical double layer declines due to a rise in the electroosmosis parameter. *CuO*-MoS_2 -Cu/Blood tri-hybrid nanofluid demonstrates greater effectiveness in regulating blood temperature compared to *CuO*-MoS_2 /Blood hybrid nanofluid. Furthermore,the influence of the Hartmann number on heat propagation is shown in Fig. 3d.

5.2. Microrotation

Vortex viscosity parameter (R_v): The relationship between the R_v and the microrotation ($g(\chi)$) of blood is shown in Fig. 4a. As R_v upsurges, it is shown that the $g(\chi)$ of blood particles throughout the arterial channel becomes more pronounced. A higher rotational speed of blood particles

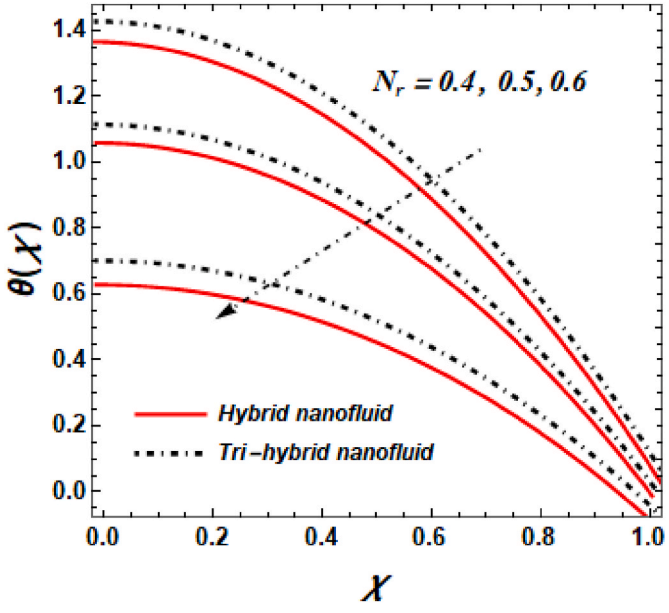


Fig. 3a. Effect of Nr on $\theta(\chi)$.

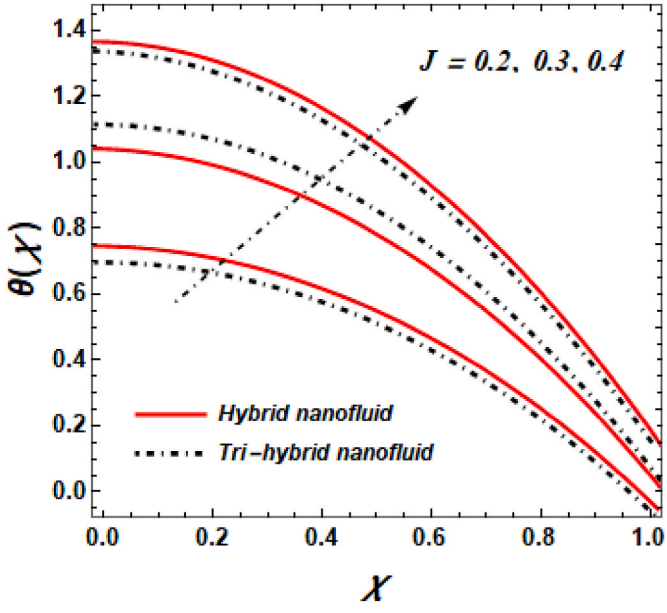


Fig. 3b. Effect of J on $\theta(\chi)$.

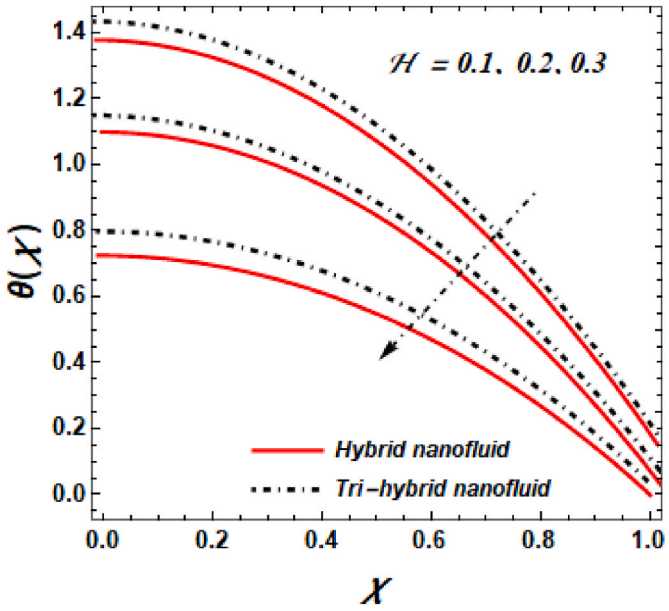


Fig. 3c. Effect of $\mathscr{H}$ on $\theta(\chi)$.

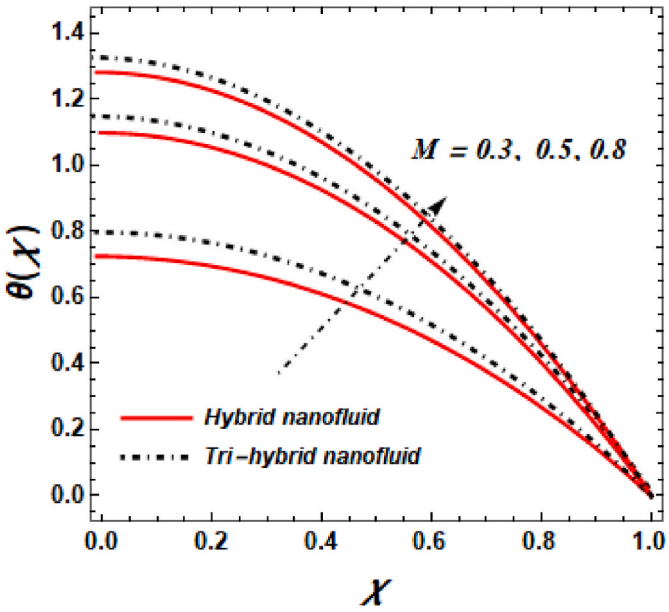


Fig. 3d. Effect of M on $\theta(\chi)$.

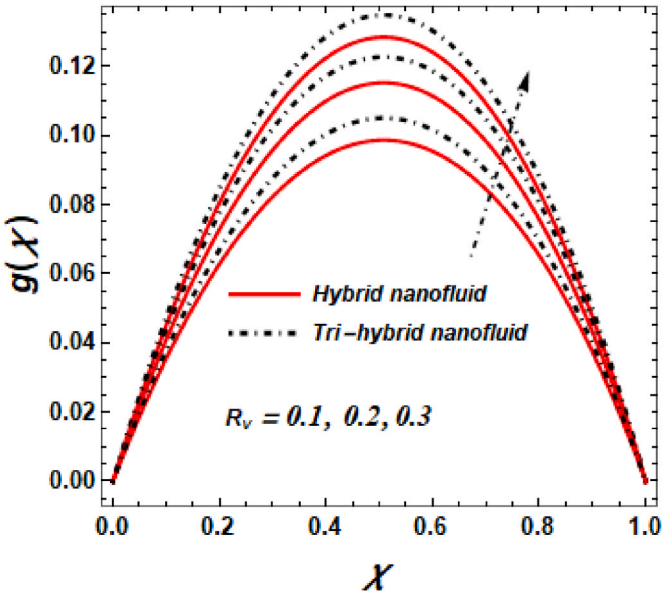


Fig. 4a. Effect of R_v on $g(\chi)$.

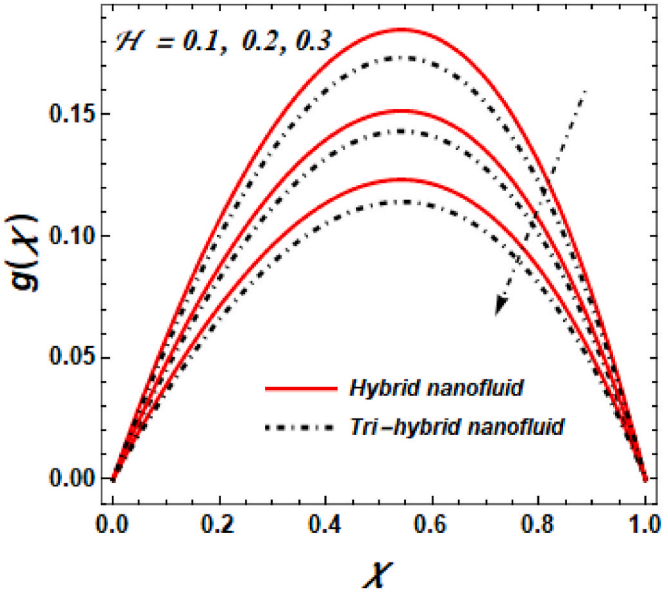


Fig. 4b. Effect of $\mathscr{H}$ on $g(\chi)$.

is caused by an increase in the value R_v. The increase in $g(\chi)$ occurs due to a rise in the viscous force exerted on the particles. The CuO-MoS_2 -Cu/Blood tri-hybrid demonstrates a greater microrotation than CuO-MoS_2 -/Blood hybrid.

Electroosmosis parameter ($\mathscr{K}$): The $g(\chi)$ displays a decreasing trend as demonstrated via the curves in Fig. 4b, showing the influence of the electroosmosis parameter. It is important to observe that the $g(\chi)$ is maximum close to the center arterial channel and progressively reduces near the channel walls. The diagram displays that rising values of the electroosmosis parameter substantially suppress the $g(\chi)$ of blood particles in the cardiovascular system. Improved liquid viscosity delays the free rotation of blood particles, which is reflected in greater inferences for the $\mathscr{K}$ parameter. The reduction in $g(\chi)$ shows that the rotational movement of the blood cell is lessened.

Micropolar parameter (η): Fig. 4c shows the influence of the η on $g(\chi)$. This $g(\chi)$ reveals a remarkable decrease as the values of micropolar parameters boost. Greater values of the η parameter are associated with increased resistance to rotational motion within the blood cell, leading to a reduced $g(\chi)$. Furthermore, the $g(\chi)$ for *CuO*-MoS_2 -Cu/Blood tri-hybrid displays greater magnitudes compared to *CuO*-MoS_2 -/Blood hybrid.

5.3. Mass Concentration

Activation energy parameter (E_a): The smallest energy required for a chemical reaction to take place is characterized via the activation energy, which is an important theory in thermodynamics and chemical kinetics. A greater value of E_a increases the mass concentration across the arterial channel. Physically, the therapeutic effectiveness of a drug can be influenced by the release or absorption rate, which may be hampered by an excessive activation energy in drug delivery. This performance is displayed in Fig. 5a.

Concentration slip parameter (C_s): The impact of C_s parameters on

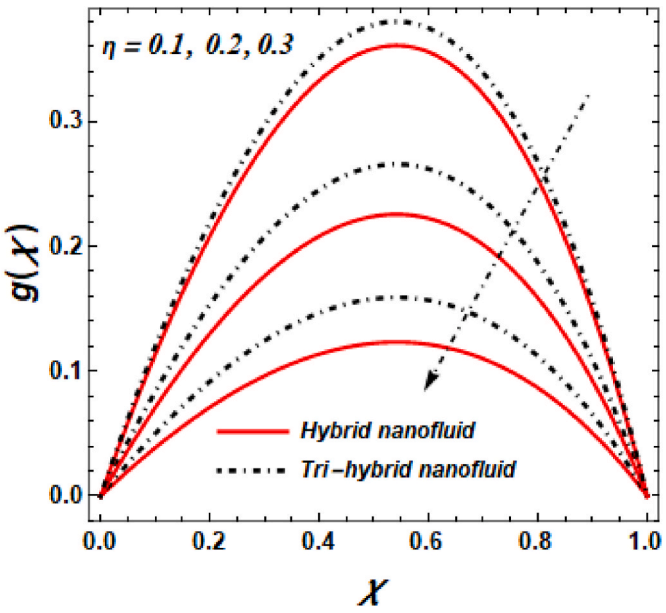


Fig. 4c. Effect of η on $g(\chi)$.

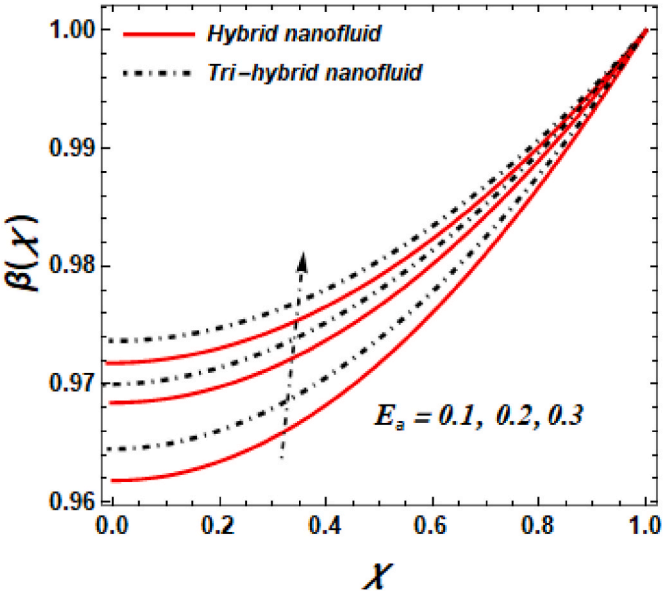


Fig. 5a. Effect of E_a on $\beta(\chi)$.

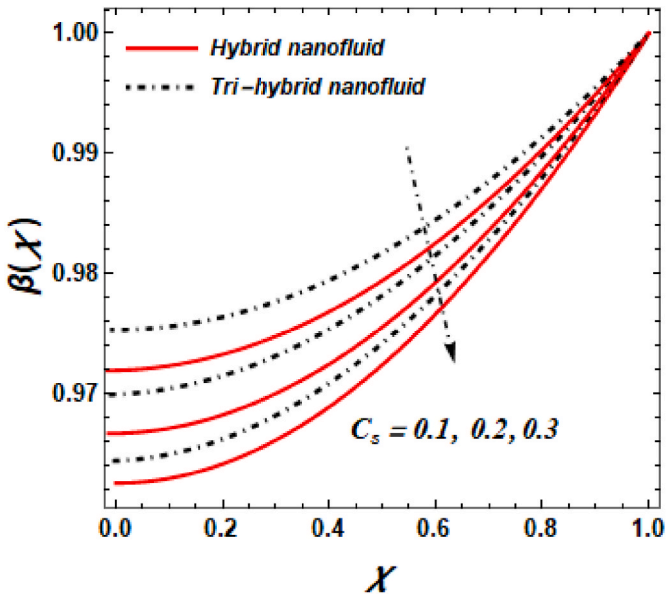


Fig. 5b. Effect of C_s on $\beta(\chi)$.

Mass Concentration are shown in Fig. 5b. The effect of the relative movement of dissolved substances at the arterial wall, compared to the blood flow velocity, is demonstrated through the use of the C_s parameters. When the slip speed of solute molecules is significantly higher compared to the speed of blood flow, it indicates that the C_s parameters are increased.

Fig. 6a presents a three-dimensional graphical representation of entropy production (GC), showing an increase in its values as Br rises. In blood flow, the importance of conductive thermal transmission compared to viscous dissipation is measured via the Br. Throughout the squeezing arterial channel, the rate of entropy production improves as Br becomes larger. Greater values of the Brinkman number display a more significant influence of viscous dissipation, leading to improved thermal conduction and, greater GC. Notably, the entropy production of the CuO-MoS_2-Cu/Blood tri-hybrid surpasses that of the CuO-MoS_2/Blood hybrid.

The influence of thermal radiation (Nr) on entropy generation (GC) can be observed in Fig. 6b. As shown in Fig. 6b, a decrease in the temperature of the *CuO*-MoS_2 -Au/Blood tri-hybrid in the arterial channel occurs with increased values of thermal radiation. A reduction in GC across the arterial channel can be seen as a result of higher values of thermal radiation. Therefore, in the arterial system, GC is significantly reduced.

6. Conclusion

In summary, this research presents a comprehensive study of the dynamical behavior of Electric Double Layers (EDL) induced on magnetized micropolar blood particles within a squeezed arterial channel, incorporating the effects of Arrhenius energy and thermal radiation mechanisms. Both the vortex viscosity and Helmholtz-Smoluchowski velocity along with the activation energy are imposed on the blood flow. This study investigates the complex behavior of blood-based tri-hybrid nanofluids incorporating copper oxide-molybdenum disulfide and copper nanoparticles. Also, this study focuses on understanding the flow dynamics, entropy generation, solute concentration, microrotation, and temperature distribution under different conditions. These models are solved numerically. Outlined below are the key results of this analysis.

- The growing values of the Hartmann number tend to increase the temperature distribution of tri-hybrid nanofluids.
- With increasing electroosmosis parameters and volume fraction of nanoparticles, the flow velocity distribution decreases.
- The Hartmann number and the Joule heating parameter both play a significant role in enhancing the heat transfer rate in nanofluids.
- For increasing values of the thermal radiation, the temperature distribution declines.
- For applications in industry that demand substantial heat transfer, ternary nanofluid might be more advantageous than hybrid nanofluid, which is typically used for considerable heat transmission.
- The microrotation field declines due to a rise in the Vortex viscosity parameter.

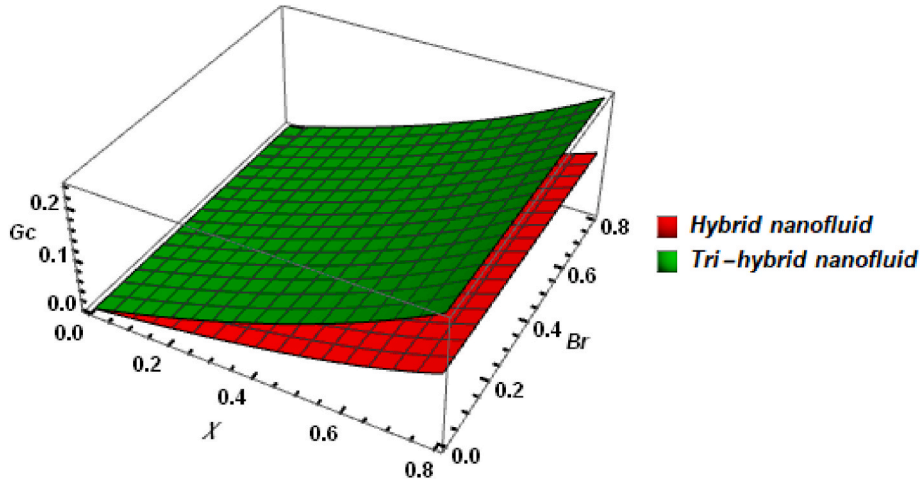


Fig. 6a. Effect of Br on Gc.

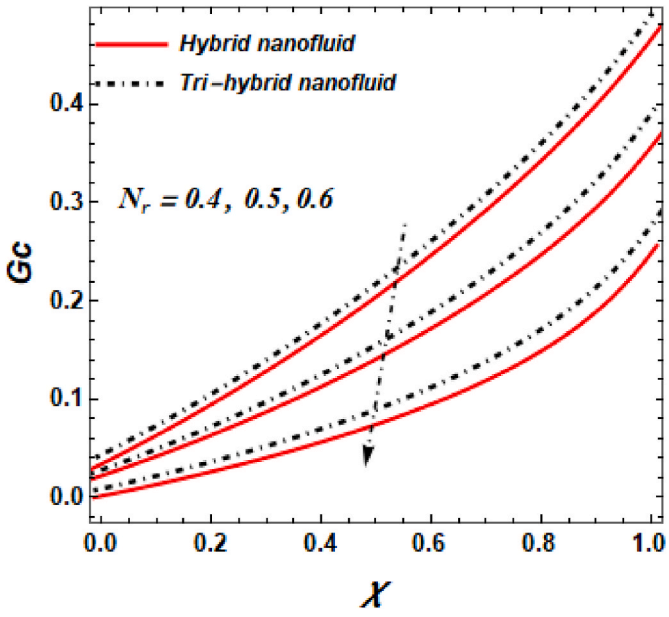


Fig. 6b. Effect of Nr on Gc.

Future recommendation

The current study focuses on specific hybrid nanofluids, but future work could explore the effects of other nanofluid compositions. Different nanoparticles, base fluids, and their interaction under varying conditions may offer more effective ways to control blood flow properties, potentially leading to improved outcomes in medical technologies such as biosensors and targeted drug delivery systems.

CRediT authorship contribution statement

A.M. Obalalu: Writing – original draft, Validation, Software, Methodology, Formal analysis, Conceptualization. **Umair Khan:** Writing – review & editing, Writing – original draft, Supervision, Resources, Conceptualization. **Mehboob Ul Hassan:** Writing – review & editing, Validation, Project administration, Investigation, Funding acquisition, Formal analysis. **Muhammad Waqas:** Writing – original draft, Validation, Software, Methodology, Formal analysis, Conceptualization. **A.D. Adeshola:** Writing – original draft, Visualization, Validation, Investigation, Data curation. **Latif Ahmad:** Writing – original draft, Visualization, Validation, Investigation, Data curation.

Data availability statement

All data are available within the manuscript.

Conflicts of interest

It is declared that we have no conflict of interest.

Acknowledgment

The authors appreciate the support of the Researchers Supporting Project number (RSPD2025R997), King Saud University, Riyadh, Saudi Arabia.

References

[1] A.C. Eringen, Theory of micropolar fluids, Journal of mathematics and Mechanics (1966) 1–18.
[2] Z. Cheng, H. Li, C. Chen, X. Lv, E. Zuo, X. Xie, C. Chen, Application of serum SERS technology based on thermally annealed silver nanoparticle composite substrate in breast cancer, Photodiagnosis Photodyn. Ther. 41 (2023) 103284, https://doi.org/10.1016/j.pdpdt.2023.103284.
[3] M. Ferdows, D. Liu, Natural convective flow of a magneto-micropolar fluid along a vertical plate, Propulsion and Power Research 7 (1) (2018) 43–51.
[4] P. Kumar Yadav, S. Jaiswal, T. Asim, R. Mishra, Influence of a magnetic field on the flow of a micropolar fluid sandwiched between two Newtonian fluid layers through a porous medium, The European Physical Journal Plus 133 (2018) 1–13.
[5] K.A. Kumar, V. Sugunamma, N. Sandeep, M. Mustafa, Simultaneous solutions for first order and second order slips on micropolar fluid flow across a convective surface in the presence of Lorentz force and variable heat source/sink, Sci. Rep. 9 (1) (2019) 14706.
[6] M.M. Khader, R.P. Sharma, Evaluating the unsteady MHD micropolar fluid flow past stretching/shirking sheet with heat source and thermal radiation: implementing fourth order predictor–corrector FDM, Math. Comput. Simulat. 181 (2021) 333–350.
[7] A.M. Obalalu, S.H.A.M. Shah, A. Darvesh, U. Khan, A. Ishak, P. Adegbite, A. M. Galal, Insight into the Hamilton and Crosser model for ternary hybrid nanofluid flow over a Riga wedge with heterogeneous catalytic reaction, Eur. Phys. J. Spec. Top. (2024) 1–22.
[8] H. Wang, B. Li, Y. Sun, Q. Ma, Y. Feng, Y. Jia, Y. Liao, NIR-II AIE luminogen-based erythrocyte-like nanoparticles with granuloma-targeting and self-oxygenation characteristics for combined phototherapy of tuberculosis, Adv. Mater. 36 (38) (2024) 2406143, https://doi.org/10.1002/adma.202406143.
[9] A.M. Obalalu, A. Darvesh, A. Abbas, A. Eladeb, R. Alsayegh, W. Rajhi, L. Kolsi, Improving solar HVAC performance by incorporating sutterby SiO2–Cu/C3H8O2 hybrid nanofluid flow via a collocation based Gegenbauer wavelets technique: effects of electromagnetic control and Smoluchowksi's temperature slippage, ZAMM-Journal of Applied Mathematics and Mechanics/Zeitschrift für Angewandte Mathematik und Mechanik (2024) e202400473.
[10] E.O. Fatunmbi, A.M. Obalalu, U. Khan, S.M. Hussain, T. Muhammad, Model development and heat transfer characteristics in renewable energy systems

conveying hybrid nanofluids subject to nonlinear thermal radiation, Multidiscip. Model. Mater. Struct. 20 (6) (2024) 1328–1342.
[11] S.O. Salawu, A.M. Obalalu, M.D. Shamshuddin, Nonlinear solar thermal radiation efficiency and energy optimization for magnetized hybrid Prandtl–Eyring nanoliquid in aircraft, Arabian J. Sci. Eng. 48 (3) (2023) 3061–3072.
[12] G.K. Ramesh, J.K. Madhukesh, N.A. Shah, S.J. Yook, Flow of hybrid CNTs past a rotating sphere subjected to thermal radiation and thermophoretic particle deposition, Alex. Eng. J. 64 (2023) 969–979.
[13] W. Wang, C. Liu, J. Luo, L. Lei, M. Chen, Y. Zhang, S. Si, A novel small-molecule PCSK9 inhibitor E28362 ameliorates hyperlipidemia and atherosclerosis, Acta Pharmacol. Sin. 45 (10) (2024) 2119–2133, https://doi.org/10.1038/s41401-024-01305-9.
[14] S. Dolui, B. Bhaumik, S. De, Combined effect of induced magnetic field and thermal radiation on ternary hybrid nanofluid flow through an inclined catheterized artery with multiple stenosis, Chem. Phys. Lett. 811 (2023) 140209.
[15] T. Mukhtar, W. Jamshed, A. Aziz, W. Al-Kouz, Computational investigation of heat transfer in a flow subjected to magnetohydrodynamic of Maxwell nanofluid over a stretched flat sheet with thermal radiation, Numer. Methods Part. Differ. Equ. 39 (5) (2023) 3499–3519.
[16] M. Waqas, U. Khan, A. Zaib, A. Ishak, M.D. Albaqami, I. Waini, I. Pop, Radiation effect on MHD three-dimensional stagnation-point flow comprising water-based graphene oxide nanofluid induced by a nonuniform heat source/sink over a horizontal plane surface, Int. J. Mod. Phys. B 37 (15) (2023) 2350146.
[17] A.M. Obalalu, Heat and mass transfer in an unsteady squeezed Casson fluid flow with novel thermophysical properties: analytical and numerical solution, Heat Transfer 50 (8) (2021) 7988–8011.
[18] J. Luo, L. Wang, C. Cui, H. Chen, W. Zeng, X. Li, MicroRNA-19a-3p inhibits endothelial dysfunction in atherosclerosis by targeting JCAD, BMC Cardiovasc. Disord. 24 (1) (2024) 394, https://doi.org/10.1186/s12872-024-04063-y.
[19] Y.M. Chu, S. Bashir, M. Ramzan, M.Y. Malik, Model-based comparative study of magnetohydrodynamics unsteady hybrid nanofluid flow between two infinite parallel plates with particle shape effects, Math. Methods Appl. Sci. 46 (10) (2023) 11568–11582.
[20] D.K. Mandal, N. Biswas, N.K. Manna, R.S.R. Gorla, A.J. Chamkha, Hybrid nanofluid magnetohydrodynamic mixed convection in a novel W-shaped porous system, Int. J. Numer. Methods Heat Fluid Flow 33 (2) (2023) 510–544.
[21] K. Hosseinzadeh, M.R. Mardani, M. Paikar, A. Hasibi, T. Tavangar, M. Nimafar, M. B. Shafii, Investigation of second grade viscoelastic non-Newtonian nanofluid flow on the curve stretching surface in presence of MHD, Results in Engineering 17 (2023) 100838.
[22] M.M. Bhatti, M.B. Arain, A. Zeeshan, R. Ellahi, M.H. Doranehgard, Swimming of Gyrotactic Microorganism in MHD Williamson nanofluid flow between rotating circular plates embedded in porous medium: application of thermal energy storage, J. Energy Storage 45 (2022) 103511.
[23] M. Arshad, A. Hussain, A. Hassan, P. Wróblewski, A. Elfasakhany, M.A. Elkotb, A. M. Galal, Thermal energy investigation of magneto-hydrodynamic nano-material liquid flow over a stretching sheet: comparison of single and composite particles, Alex. Eng. J. 61 (12) (2022) 10453–10462.
[24] a H. Gasmi, A.O. Akindele, A.M. Obalalu, A.A. Usman, U. Khan, Y. Yilmaz, N. Nizampatnam, Electromagnetic control and heat transfer enhancement in exothermic reactions experiencing current density: the study preventing thermal explosions in reactive flow, Appl. Rheol. 34 (1) (2024) 20240020;
b G.A. Al-Turef, A.M. Obalalu, W. Saleh, S.H.A.M. Shah, A. Darvesh, U. Khan, S. M. Hussain, Computational study and application of the Hamilton and crosser model for ternary hybrid nanofluid flow past a riga wedge with heterogeneous catalytic reaction, Nano (2024) 2450105.
[25] A. Dawar, Z. Shah, H.M. Alshehri, S. Islam, P. Kumam, Magnetized and non-magnetized Casson fluid flow with gyrotactic microorganisms over a stratified stretching cylinder, Sci. Rep. 11 (1) (2021) 16376.
[26] D. Kumar, B. Satyanarayana, R. Kumar, S. Kumar, N. Deo, Application of heat source and chemical reaction in MHD blood flow through permeable bifurcated arteries with inclined magnetic field in tumor treatments, Results in Applied Mathematics 10 (2021) 100151.
[27] R. Ponnalagarsamy, M. Kawahara, A finite element analysis of laminar unsteady flow of viscoelastic fluids through channels with non-uniform cross-sections, Int. J. Numer. Methods Fluid. 9 (12) (1989) 1487–1501.
[28] S. Priyadharshini, R. Ponalagusamy, Computational model on pulsatile flow of blood through a tapered arterial stenosis with radially variable viscosity and magnetic field, Sādhanā 42 (2017) 1901–1913.
[29] P. Chaturani, R. Ponnalagarsamy, Analysis of pulsatile blood flow through stenosed arteries and its applications to cardiovascular diseases, in: Proceedings of the 13th National Conference on Fluid Mechanics and Fluid Power (*FMFP*-1984), 1984, pp. 463–468.
[30] S. Noreen, F. Aslam, Electro-osmotic mechanism of Ellis fluid with joule heating, viscous dissipation, and magnetic field effects in a pumping microtube, J. Biomech. Eng. 147 (1) (2025).
[31] S. Noreen, F. Aslam, Electro-osmotic mechanism of Ellis fluid with joule heating, viscous dissipation, and magnetic field effects in a pumping microtube, J. Biomech. Eng. 147 (1) (2025).
[32] P. Senbagaraja, P. De, Sensitivity analysis on electro-osmotic flow of EMHD tangent hyperbolic nanofluid through porous rotating disk with variable thermal conductivity, Stefan blowing and thermal radiation, Multiscale and Multidisciplinary Modeling, Experiments and Design 8 (1) (2025) 65.
[33] I. Waini, A. Ishak, I. Pop, MHD flow and heat transfer of a hybrid nanofluid past a permeable stretching/shrinking wedge, Appl. Math. Mech. 41 (3) (2020) 507–520.
[34] O.A. Olayemi, K. Al-Farhany, A.M. Obalalu, T.F. Ajide, K.R. Adebayo, Magnetoconvection around an elliptic cylinder placed in a lid-driven square enclosure subjected to internal heat generation or absorption, Heat Transfer 51 (6) (2022) 4950–4976.
[35] A.M. Khan, M.K. Gupta, H. Hegab, M. Jamil, M. Mia, N. He, C.I. Pruncu, Energy-based cost integrated modelling and sustainability assessment of Al-GnP hybrid nanofluid assisted turning of AISI52100 steel, J. Clean. Prod. 257 (2020) 120502.
[36] N. Abbas, S. Nadeem, A. Saleem, M.Y. Malik, A. Issakhov, F.M. Alharbi, Models base study of inclined MHD of hybrid nanofluid flow over nonlinear stretching cylinder, Chin. J. Phys. 69 (2021) 109–117.
[37] J.K. Madhukesh, R.N. Kumar, R.P. Gowda, B.C. Prasannakumara, G.K. Ramesh, M. I. Khan, Y.M. Chu, Numerical simulation of AA7072-AA7075/water-based hybrid nanofluid flow over a curved stretching sheet with Newtonian heating: a non-Fourier heat flux model approach, J. Mol. Liq. 335 (2021) 116103.
[38] G. Sadeghi, S. Nazari, Retrofitting a thermoelectric-based solar still integrated with an evacuated tube collector utilizing an antibacterial-magnetic hybrid nanofluid, Desalination 500 (2021) 114871.
[39] Pullare Nimmy, Adebowale Martins Obalalu, Kallur Venkat Nagaraja, Javali Kotresh Madhukesh, Umair Khan, Anuar Ishak, Devanathan Sriram, Syed Modassir Hussain, Raman Kumar, Ahmed M. Abed, Computational analysis of nanoparticles and waste discharge concentration past a rotating sphere with Lorentz forces, Appl. Rheol. 34 (1) (2024) 20240012.
[40] A.M. Obalalu, T. Oreyeni, A. Abbas, M.A. Memon, U. Khan, E.S.M. Sherif, I. Pop, Implication of electromagnetohydrodynamic and heat transfer analysis in nanomaterial flow over a stretched surface: applications in solar energy, Case Stud. Therm. Eng. 49 (2023) 103381.
[41] M. Nadeem, I. Siddique, J. Awrejcewicz, M. Bilal, Numerical analysis of a second-grade fuzzy hybrid nanofluid flow and heat transfer over a permeable stretching/shrinking sheet, Sci. Rep. 12 (1) (2022) 1631.
[42] Z. Shah, M. Rooman, M. Shutaywi, Computational analysis of radiative engine oil-based Prandtl–Eyring hybrid nanofluid flow with variable heat transfer using the Cattaneo–Christov heat flux model, RSC Adv. 13 (6) (2023) 3552–3560.
[43] R. Akhter, M.M. Ali, M.A. Alim, Entropy generation due to hydromagnetic buoyancy-driven hybrid-nanofluid flow in partially heated porous cavity containing heat conductive obstacle, Alex. Eng. J. 62 (2023) 17–45.
[44] A.M. Obalalu, M.O. Oni, U. Khan, A. Abbas, T. Muhammad, A. Zaib, Two-phase numerical simulation for the heat and mass transfer evaluation across a vertical deformable sheet with significant impact of solar radiation and heat source/sink, Arabian J. Sci. Eng. 49 (8) (2024) 11053–11071.
[45] U. Khan, A.M. Obalalu, A. Zaib, A. Ishak, S.M. Hussain, J.K. Madhukesh, A. M. Galal, Irreversibility analysis of cross-flow in Eyring–Powell nanofluid over a permeable deformable sheet with Lorentz forces, ZAMM-Journal of Applied Mathematics and Mechanics/Zeitschrift für Angewandte Mathematik und Mechanik (2024) e202300835.
[46] D. Toghraie, N.N. Esfahani, M. Zarringhalam, N. Shirani, S. Rostami, Blood flow analysis inside different arteries using non-Newtonian Sisko model for application in biomedical engineering, Comput. Methods Progr. Biomed. 190 (2020) 105338.
[47] S.R. Yan, M. Zarringhalam, D. Toghraie, L.K. Foong, P. Talebizadehsardari, Numerical investigation of non-Newtonian blood flow within an artery with cone shape of stenosis in various stenosis angles, Comput. Methods Progr. Biomed. 192 (2020) 105434.
[48] X. Liu, X. Chen, Y. Zhang, J. Xie, X. Jia, T. Deng, Z. Majid, The thermal behavior of blood flow in the arteries with various radii and various stenosis angles using non-Newtonian Sisko model, Alex. Eng. J. 61 (9) (2022) 7195–7201.
[49] A. Karimipour, D. Toghraie, L.A. Abdulkareem, A.A. Alizadeh, M. Zarringhalam, A. Karimipour, Roll of stenosis severity, artery radius and blood fluid behavior on the flow velocity in the arteries: application in biomedical engineering, Med. Hypotheses 144 (2020) 109864.
[50] M. Bao, G. Li, X. Huang, L. Tang, L. Dong, J. Li, Long noncoding RNA LINC00657 acting as a miR-590-3p sponge to facilitate low concentration oxidized low-density lipoprotein–induced angiogenesis, Mol. Pharmacol. 93 (4) (2018) 368–375, https://doi.org/10.1124/mol.117.110650.
[51] J. Tang, J. Li, G. Li, H. Zhang, L. Wang, D. Li, J. Ding, Spermidine-mediated poly (lactic-co-glycolic acid) nanoparticles containing fluorofenidone for the treatment of idiopathic pulmonary fibrosis, Int. J. Nanomed. 12 (2017) 6687–6704, https://doi.org/10.2147/IJN.S140569.
[52] J. Deng, Q. Liu, L. Ye, S. Wang, Z. Song, M. Zhu, T. Chen, The Janus face of mitophagy in myocardial ischemia/reperfusion injury and recovery, Biomed. Pharmacother. 173 (2024) 116337.
[53] P. Paul, P. Karmakar, S. Das, S. Das, Demonstration of angioplasty using a balloon catheter in tetra-hybrid nano-bloodstream within an electrified stenotic arterial cavity under a magnetic field: artificial neural network analysis, Biomed. Signal Process Control 96 (2024) 106549.
[54] S. Das, S. Das, Exploring stream patterns of titania-CNTs blended blood in a squeezed artery subject to electro-magnetization, Hall and ion-slip currents, Int. J. Biomath. (IJB) (2024).
[55] P. Karmakar, S. Das, A neural network approach to explore bioelectromagnetics aspects of blood circulation conveying tetra-hybrid nanoparticles and microbes in a ciliary artery with an endoscopy span, Eng. Appl. Artif. Intell. 133 (2024) 108298.
[56] A. Ali, S. Das, Applications of neuro-computing and fractional calculus to blood streaming conveying modified trihybrid nanoparticles with interfacial nanolayer aspect inside a diseased ciliated artery under electroosmotic and Lorentz forces, Int. Commun. Heat Mass Tran. 152 (2024) 107313.
[57] P. Karmakar, S. Das, EDL induced electro-magnetized modified hybrid nano-blood circulation in an endoscopic fatty charged arterial indented tract, Cardiovascular Engineering and Technology 15 (2) (2024) 171–198.

[58] S. Das, S. Das, EDL impelled flow of magnetized micropolar CNTs-Ingrained blood through a squeezed arterial channel, BioNanoScience 14 (1) (2024) 119–152.
[59] S. Das, S. Das, EDL aspects in swirling ionic tribological fluid flow in a squeezed/split channel underlie a high-power magnetic field, Forces in Mechanics 11 (2023) 100196.
[60] O.A. Bég, D. Kumar, M.J. Uddin, M.A. Alim, T.A. Bég, Simulation of magneto-nano-bioconvective coating flow with blowing and multiple slip effects. Proceedings of the Institution of Mechanical Engineers, Part N: Journal of Nanomaterials, Nanoengineering and Nanosystems, 2024 23977914241259815.
[61] W.A. Khan, M.J. Uddin, Nano-bioconvective anisotropic slip flow in anisotropic porous medium with Coriolis force effects, Heat Transfer 53 (2) (2024) 558–583.
[62] M.J. Uddin, P. Rana, S. Gupta, M.N. Uddin, Bio-nanoconvective micropolar fluid flow in a Darcy porous medium past a cone with second-order slips and stefan blowing: FEM solution, Iranian Journal of Science and Technology, Transactions of Mechanical Engineering 47 (4) (2023) 1633–1647.
[63] M.A.A. Hamad, M.J. Uddin, A.M. Ismail, Investigation of combined heat and mass transfer by Lie group analysis with variable diffusivity taking into account hydrodynamic slip and thermal convective boundary conditions, Int. J. Heat Mass Tran. 55 (4) (2012) 1355–1362.
[64] N.A. Amirsom, M.J. Uddin, M.F.M. Basir, A.I.M. Ismail, O.A. Bég, A. Kadir, Three-dimensional bioconvection nanofluid flow from a bi-axial stretching sheet with anisotropic slip, Sains Malays. 48 (5) (2019) 1137–1149.
[65] M.J. Uddin, O. Anwar Bég, M.N. Uddin, Multiple slips and variable transport property effect on magnetohydromagnetic dissipative thermosolutal convection in a porous medium, J. Aero. Eng. 29 (5) (2016) 04016024.
[66] M.J. Uddin, O.A. Bég, S. Kuharat, Computation of rheological nanofluid coating boundary layer transport with convective wall heating. Proceedings of the Institution of Mechanical Engineers, Part N: Journal of Nanomaterials, Nanoengineering and Nanosystems, 2024 23977914241270892.
[67] M.J. Uddin, O.A. Bég, A.I. Ismail, Radiative convective nanofluid flow past a stretching/shrinking sheet with slip effects, J. Thermophys. Heat Tran. 29 (3) (2015) 513–523.
[68] R. Ponalagusamy, A two-layered suspension (particle-fluid) model for non-Newtonian fluid flow in a catheterized arterial stenosis with slip condition at the wall of stenosed artery, Korea Aust. Rheol. J. 29 (2017) 87–100.
[69] R. Ponalagusamy, J. Sangeetha, Electroosmotic effect on two immiscible (conducting–non-conducting) fluids flowing in the porous channel under magnetic field, Proc. IME E J. Process Mech. Eng. 237 (5) (2023) 2029–2044.
[70] P. Ramasamy, Effects of magnetic force and non-Newtonian characteristics on squeeze film bearings, Asia Pac. J. Chem. Eng. 15 (5) (2020) e2510.
[71] R. Ponalagusamy, Particulate suspension Jeffrey fluid flow in a stenosed artery with a particle-free plasma layer near the wall, Korea Aust. Rheol. J. 28 (2016) 217–227.
[72] N.N. Kumar, D.R.V.S.R.K. Sastry, S. Shaw, Irreversibility analysis of an unsteady micropolar CNT-blood nano-fluid flow through a squeezing channel with activation energy-application in drug delivery, Comput. Methods Progr. Biomed. 226 (2022) 107156.
[73] S. Das, S. Das, EDL aspects in swirling ionic tribological fluid flow in a squeezed/split channel underlie a high-power magnetic field, Forces in Mechanics 11 (2023) 100196.